# Ventilation of the deep Southern Ocean and deglacial CO_2 rise

Luke C. Skinner, Stewart J. Fallon, C. Waelbroeck, Elisabeth Michel, Stephen Barker

# Ventilation of the Deep Southern Ocean and Deglacial $CO_2$ Rise

L. C. Skinner,[1]* S. Fallon,[2] C. Waelbroeck,[3] E. Michel,[3] S. Barker[4]

Past glacial-interglacial increases in the concentration of atmospheric carbon dioxide ($CO_2$) are thought to arise from the rapid release of $CO_2$ sequestered in the deep sea, primarily via the Southern Ocean. Here, we present radiocarbon evidence from the Atlantic sector of the Southern Ocean that strongly supports this hypothesis. We show that during the last glacial period, deep water circulating around Antarctica was more than two times older than today relative to the atmosphere. During deglaciation, the dissipation of this old and presumably $CO_2$-enriched deep water played an important role in the pulsed rise of atmospheric $CO_2$ through its variable influence on the upwelling branch of the Antarctic overturning circulation.

There is a broad consensus that glacial-interglacial atmospheric carbon dioxide ($CO_2$) change depends primarily on marine processes operating in the Southern Ocean (*1*–*3*). The special importance of this region is suggested by the observed link between atmospheric $CO_2$ and Antarctic temperature change on both orbital and millennial time scales (*4*, *5*). However, the expectation of a Southern Ocean role in past $CO_2$ variability is also based on strong conceptual grounds because this is the region of the global ocean where most deep water makes its first contact with the sea surface (*6*), and consequently where $CO_2$ that has accumulated in the deep sea can be released to the atmosphere.

One important clue regarding the ocean's potential role in atmospheric $CO_2$ variability comes from the record of atmospheric radiocarbon activity ($\Delta^{14}C_{atm}$), which reveals an apparent "excess" of atmospheric $^{14}C$ during the last glacial period relative to the present and relative to concurrent $^{14}C$ production rates (*7*). This apparent $\Delta^{14}C_{atm}$ excess was eliminated across the last deglaciation in two steps (*8*, *9*), each of which coincided with a sharp rise in atmospheric $CO_2$ (*10*) (Fig. 1, vertical lines). The widely held expectation is therefore that lowered glacial $CO_2$ and the rapid deglacial $CO_2$ rise were made possible by the sequestration of an aged, carbon-rich deep-water mass that was mixed with the atmosphere in two pulses across the deglaciation.

Although this expectation, referred to here as the "deep re-coupling hypothesis," is compelling and circumstantially supported (*2*, *11*), it has yet to be confirmed directly through marine $^{14}C$ ventilation reconstructions. For example, available $^{14}C$ evidence from the deep Pacific appears to restrict the putative aged carbon reservoir to depths of >2.8 km in this basin (*8*, *12*). Other marine $^{14}C$ evidence from the North Pacific and North Atlantic suggests at the very least the existence of strong $^{14}C$ activity gradients within the glacial ocean (*9*, *11*, *13*, *14*). The oldest water body thus identified was more than 3000 years offset from the atmosphere (*11*), although its existence and extent during the glacial before ~18 thousand years before the present (ky B.P.) remains unconfirmed. Indeed, none of the available marine $^{14}C$ reconstructions reveal the occurrence of a relatively aged and widely exported deep-water mass before the initiation of the so-

[1]Godwin Laboratory for Palaeoclimate Research, Department of Earth Sciences, University of Cambridge, Downing Street, Cambridge CB2 3EQ, UK. [2]Research School of Earth Sciences, Australian National University (ANU), Canberra ACT 0200, Australia. [3]Laboratoire des Sciences du Climat et l'Environnement/Institut Pierre-Simon Laplace, Laboratoire CNRS-CEA-UVSQ, Bâtiment 12, Avenue de la Terrasse, F-91198, Gif-sur-Yvette Cedex, France. [4]School of Earth and Ocean Sciences, Cardiff University, Cardiff CF10 3YE, UK.

*To whom correspondence should be addressed. E-mail: lcs32@esc.cam.ac.uk

called "mystery interval" [approximately equivalent to Heinrich Stadial 1 (HS1)] at ~17.9 ky B.P., when atmospheric $CO_2$ began to rise and $\Delta^{14}C_{atm}$ began to drop sharply (*8*). Here, we bridge precisely this gap by demonstrating the existence during the last glaciation of a poorly ventilated carbon pool deep in the Atlantic sector of the Southern Ocean that dissipated in two pulses across the deglaciation.

Radiocarbon analyses were performed on paired samples of (monospecific) planktonic and (mixed) benthic foraminifera from core MD07-3076 CQ (44° 4.46'S, 14°12.47'W, 3770 m). All $^{14}C$ samples were subjected to a rigorous cleaning procedure so as to eliminate all adhering phases other than primary carbonate (*15*). Auxiliary Mg/Ca analyses were performed on samples of the planktonic foraminifer species *Globigerina bulloides* and *Neogloboquadrina pachyderma* (left coiling) from the same core (*15*).

The site of MD07-3076 (fig. S1) currently lies on the locus of water that is spread throughout the ocean via upper-ocean and abyssal circulation limbs (*15*). It is expected that this site experienced less North Atlantic Deep Water (NADW) influence during the last glaciation, such as in the deep Cape Basin (*16*), while nevertheless remaining on the deep-water "umbilicus" that links the Atlantic with the immense Indo-Pacific.

The chronology for core MD07-3076 is based on 59 monospecific planktonic foraminifer accelerator mass spectrometry (AMS) $^{14}C$ dates that have been corrected for variable reservoir age effects. We applied two independent methods to constrain local reservoir age variability. First, Antarctic ice-core ages obtained via correlation of Antarctic and local sea-surface temperature trends (fig. S3) were used to derive reservoir age ranges at stratigraphic tie-points (*15*). These estimates were verified against surface reservoir ages that were inferred independently from the published chronology for core TNO57-21 (Cape Basin) (*3*). Both methods yield strikingly similar histories of reservoir age variability at the site of MD07-3076, with a large increase in surface reservoir ages occurring during HS1 in particular. Reservoir ages at the more southerly site of MD07-3076 exceed those in the Cape Basin by ~2000 years, suggesting the northward migration of the sub-Antarctic Front (and divergence) to a position between the two cores. We derived age-depth models for multiple reservoir age scenarios using the Bayesian calibration and age-modeling program *Bchron* (*17*), providing a bounded "best estimate" reservoir age scenario and chronology that uses all available chronostratigraphic constraints (ice core and marine). The resulting chronology possesses quantifiable uncertainties and is in good agreement with two independent age scales (fig. S8).

The reconstructed deep-water ventilation/reservoir age history from core MD07-3076 is illustrated in Fig. 2D [benthic-planktonic age offsets (B-P)] and Fig. 2E [benthic-atmospheric age offsets (B-Atm)]. As shown in Fig. 2, D and E, deep water in the Atlantic sector of the Southern Ocean was poorly ventilated during the last glacial period, before HS1, reaching on average ~1630 years older than the local sea surface (B-P) and 2000 to 3750 years older than the atmosphere (B-Atm). This represents an increase of between 1.6 and 3 times relative to the modern ventilation ages (modern B-P is ~550 years, and modern B-Atm is ~1250 years) (Fig. 2, D and E). During the last glacial period, and at the Last Glacial Maximum (LGM) in particular, the time scale of carbon exchange between the atmosphere and the deep Southern Ocean therefore appears to have exceeded that of the most poorly ventilated regions of the modern deep North Pacific. All else being equal, this increase in the ventilation time scale of the deep sea would have enhanced the carbon sequestration capacity of the deep ocean during the last glacial period, thus helping to reduce atmospheric $CO_2$.

Across the deglaciation, between the LGM and the end of the Pre-Boreal/Younger Dryas (PB-YD), the influence of exceptionally aged deep water gradually decreased at the location of MD07-3076 (Fig. 2E). This long-term trend toward better-ventilated deep water occurred in parallel with a general trend toward increased atmospheric $CO_2$ (Fig. 2A), a gradual reduction in Antarctic sea-ice production (Fig. 2B), and generally more negative but increasing atmospheric $\partial^{13}CO_2$ (Fig. 2C) (*18*). This time interval also coincides with a broad $\partial^{13}C$ "minimum" recorded by planktonic foraminifera in the Eastern Equatorial Pacific (EEP), which has been interpreted to reflect a combination of increased upwelling at low latitudes and increased remineralized nutrient export from the Southern Ocean (*19*, *20*). All of these records are consistent, with a "mode shift" in the exchange of $CO_2$ between the ocean interior and the atmosphere across the last deglaciation, resulting in a tendency for greater exchange between the atmosphere and a marine carbon pool (*18*) that was especially depleted in $\partial^{13}C$ (*19*, *21*) and $\Delta^{14}C$ (Figs. 1A and 2D).

However, closer inspection of Fig. 2 also reveals that the deglacial trends in $CO_2$, Antarctic

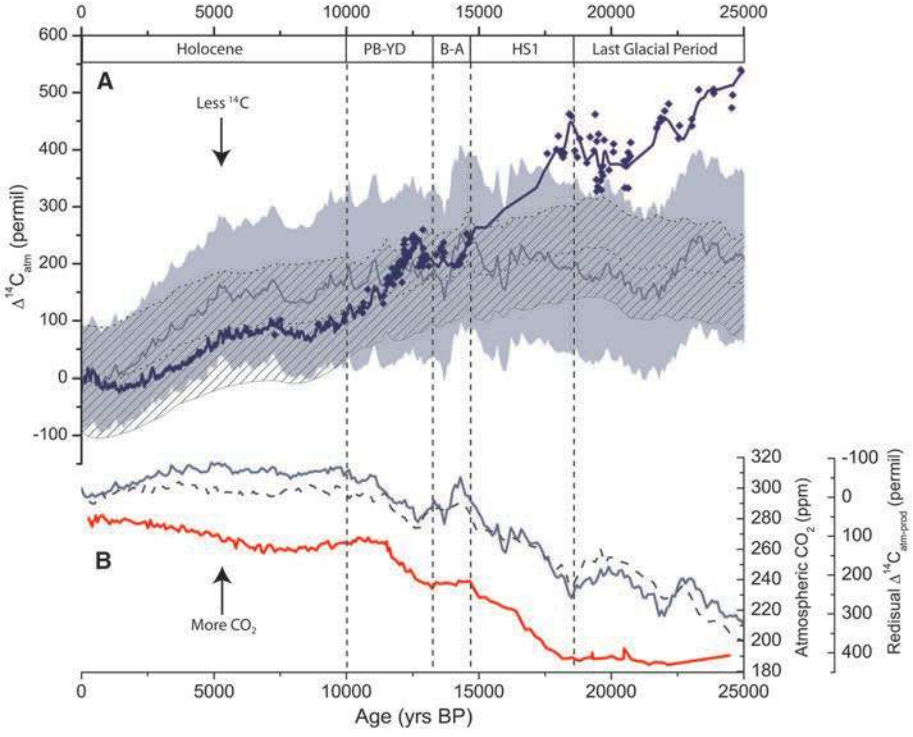


**Fig. 1.** Atmospheric $CO_2$ and radiocarbon activity ($\Delta^{14}C$) changes across the last deglaciation. (**A**) Reconstructed atmospheric $\Delta^{14}C$ [blue diamonds indicate coral data (*22*), and the blue line is the INTCAL04 calibration curve (*23*)], compared with the expected atmospheric $\Delta^{14}C$ record based only on $^{14}C$-production changes, derived using the BICYCLE model (*24*) with constant modern carbon cycling, and upper and lower $^{14}C$ production limits from Greenland ice-core $^{10}Be$ fluxes (shaded area) (*25*) and global paleomagnetic field intensity (hatched area) (*26*). (**B**) Atmospheric $CO_2$ concentrations from the European Project for Ice Coring in Antarctica (EPICA) Dome C (EDC) ice core (red line) (*10*), including one $CO_2$ measurement at 24.4 ky B.P. from the Taylor Dome ice core (*27*). The $CO_2$ data are shown here on EDML-GICC05 equivalent ages (*15*). The gray and blue lines in (B) indicate the difference between the reconstructed $\Delta^{14}C_{atm}$ record and the median simulated production histories from paleomagnetic intensity (dashed gray line) and $^{10}Be$ fluxes (solid blue line). These lines indicate atmospheric $\Delta^{14}C$ changes that may be attributed to carbon cycle changes (indicated with the inverted *y* axis). Vertical lines bound two rapid drops in atmospheric $\Delta^{14}C$, which do not coincide with similar changes in $^{14}C$-production but do coincide with rapid jumps in $CO_2$. These intervals are roughly coincident with HS1 and the YD, as indicated by the chronostratigraphic labels at the top of the graph. BA, Bølling-Allerød.

sea ice, atmospheric $\partial^{13}CO_2$, and deep-water ventilation were not monotonic. During the Antarctic Cold Reversal (ACR)/Bølling-Allerød, $CO_2$ (Fig. 2A) and $\partial^{13}CO_2$ (Fig. 2C) reversed their increasing trends, whereas $\Delta^{14}C_{atm}$ paused in its rapid decline (Fig. 1). In order to explain why these changes may have occurred, we identify three sets of conditions: (i) LGM, maximally extended Antarctic sea ice in conjunction with exceptionally aged circumpolar deep water (CDW) and stable but low $CO_2$; (ii) HS1 and YD, receding Antarctic sea ice in conjunction with relatively aged CDW and rising $CO_2$; and (iii) ACR/Bølling-Allerød, reduced but expanding Antarctic sea ice in conjunction with very young CDW and more elevated but approximately stable $CO_2$.

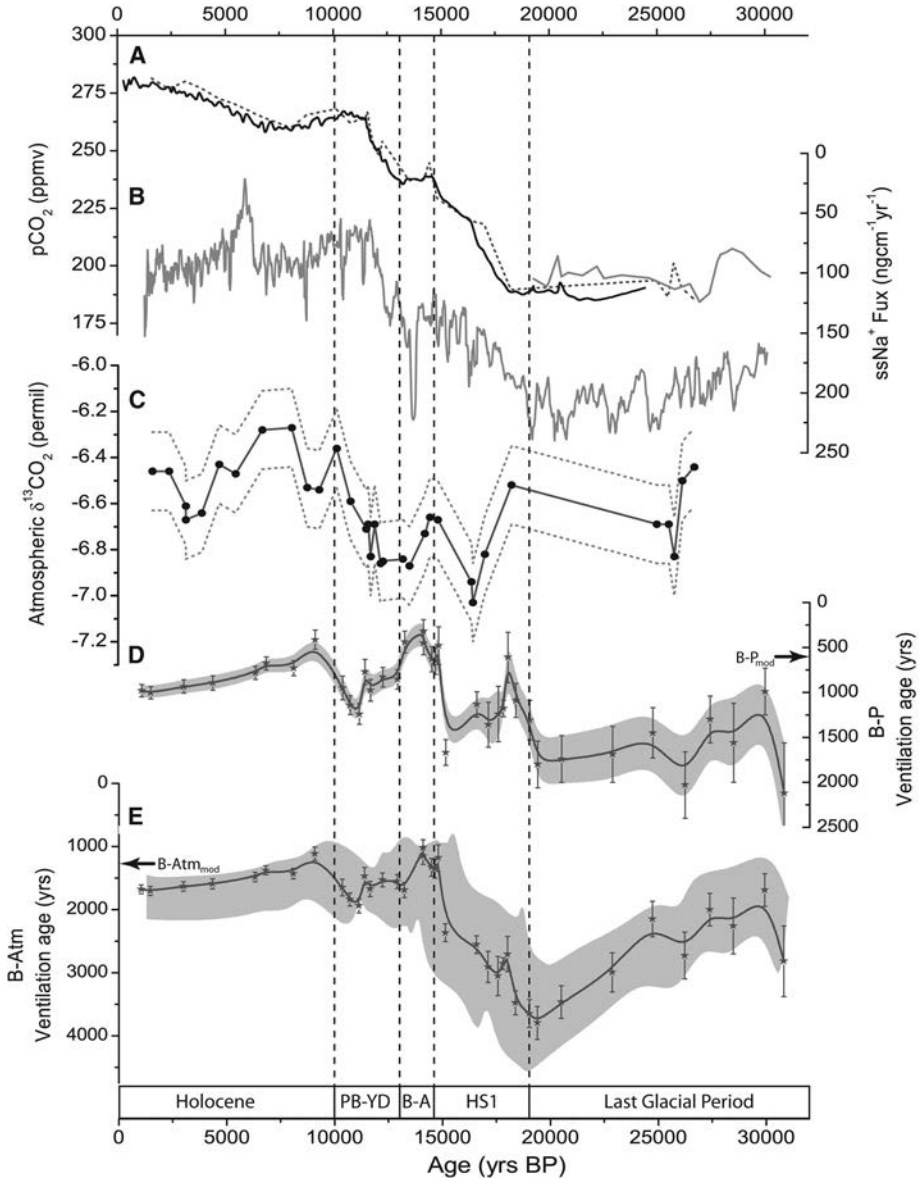


**Fig. 2.** Deep-water ventilation changes in the Atlantic sector of the Southern Ocean. (**A**) Atmospheric $CO_2$ from the EDC (*10*), Taylor Dome (*18*), and Byrd (*5*) ice cores, shown by solid dark gray, dashed, and light gray lines, respectively, and placed on the age scale of (*28*). (**B**) Sea salt–derived sodium fluxes from the EPICA Dronning Maud Land (EDML) ice core (*29*), as a regional sea-ice proxy, also on the NGRIP-GICC05 age scale. Although this is only an indirect sea ice proxy, it shows a deglacial pattern that is qualitatively similar to other marine proxy–based reconstructions. (**C**) $\partial^{13}CO_2$ measurements from the Taylor Dome Antarctic ice core (*18*), placed on the NGRIP-GICC05 age scale by alignment of $CH_4$ trends (*15*). Dotted lines indicate 2σ uncertainty range. (**D**) Benthic-planktonic $^{14}C$ age offsets in core MD07-3076 (error bars represent combined 1σ error in $^{14}C$ dates; shaded area indicates b-spline smoothed upper/lower limits of B-P defined by the 1σ error bars). (**E**) Apparent deep-water ventilation in core MD07-3076 (B-Atm). Heavy gray line (b-spline smoothed) and stars indicate the best estimate ventilation history and associated chronology. Vertical error ranges show the magnitude of combined planktonic/benthic $^{14}C$ date uncertainties (1σ). The shaded area shows the range of ventilation histories (b-spline smoothed) that could be supported by alternative surface reservoir age scenarios. Labels at the base indicate approximate timing of North Atlantic event-stratigraphy chronozones.

The associations identified above are consistent with the idea that the retraction of Antarctic sea ice from its maximal LGM extent may have increased the latitude band over which westerly winds could "stir up" CDW along steepened isopycnals, which would now outcrop increasingly to the south. This process may have been exacerbated during North Atlantic stadials (HS1 and the YD) because of an increase in the southward heat transport of the South Atlantic gyre via the "bipolar seesaw" mechanism (*2*, *3*). Although the CDW being brought to the surface in this way remained under the influence of an exceptionally aged and presumably high-potential partial pressure of $CO_2$ ($P_{CO_2}$) abyssal reservoir (water that would have high $P_{CO_2}$ when brought to the sea surface), the rate of $CO_2$ release from the Southern Ocean would have been enhanced (such as during HS1 and the YD) (Fig. 2, D and E). On the other hand, when the CDW that was being brought to the surface came under the influence of much better ventilated and presumably lower potential $P_{CO_2}$ deep water, as it did during the ACR/Bølling-Allerød (Fig. 2, D and E), the release of $CO_2$ from the Southern Ocean would have been much reduced.

The drop in ventilation ages observed in MD07-3076 approximately in time with the ACR/Bølling-Allerød (Fig. 2E) is coherent with similar features observed in the Pacific (*11*, *14*) and North Atlantic (*9*, *13*). This is shown in Fig. 3, which compares the evolution of atmospheric $\Delta^{14}C_{atm}$ with ventilation changes reconstructed for the deep Southern Ocean [MD07-3076 (this study)], the shallow east Pacific [GCMV99-GC31/PC08 (*11*)], and the deep Northeast Atlantic [MD99-2334K (*13*), supplemented here with three additional benthic $^{14}C$ dates (*15*)]. This comparison suggests that the exceptionally aged deep water that is thought to have escaped into the shallow Pacific via Antarctic Intermediate Water (AAIW) during HS1 and the YD (*11*), and that is also inferred to have been mixed into the North Atlantic at these times (*9*, *13*), was previously restricted to the deep Southern Ocean where it increasingly influenced the site of MD07-3076 as the LGM approached. It would also appear that despite its proximity to this exceptionally aged water mass, the site of MD07-3076 apparently was not (or did not remain) at its core. This is implied by the increase in ventilation ages in MD07-3076 toward the LGM and by the much higher ventilation ages observed at the shallow Pacific site between the middle of HS1 and the end of the YD (~16 to 10 ky B.P., Fig. 3B). Assuming that the shallow Pacific site is indeed representative of southern sourced water, the reversal in ventilation gradient between the two marine sites could suggest that the aged abyssal reservoir remained partially intact somewhere in the abyss until the end of the YD, despite having substantially withdrawn from the Atlantic sector of the deep Southern Ocean by this time (Fig. 2E).

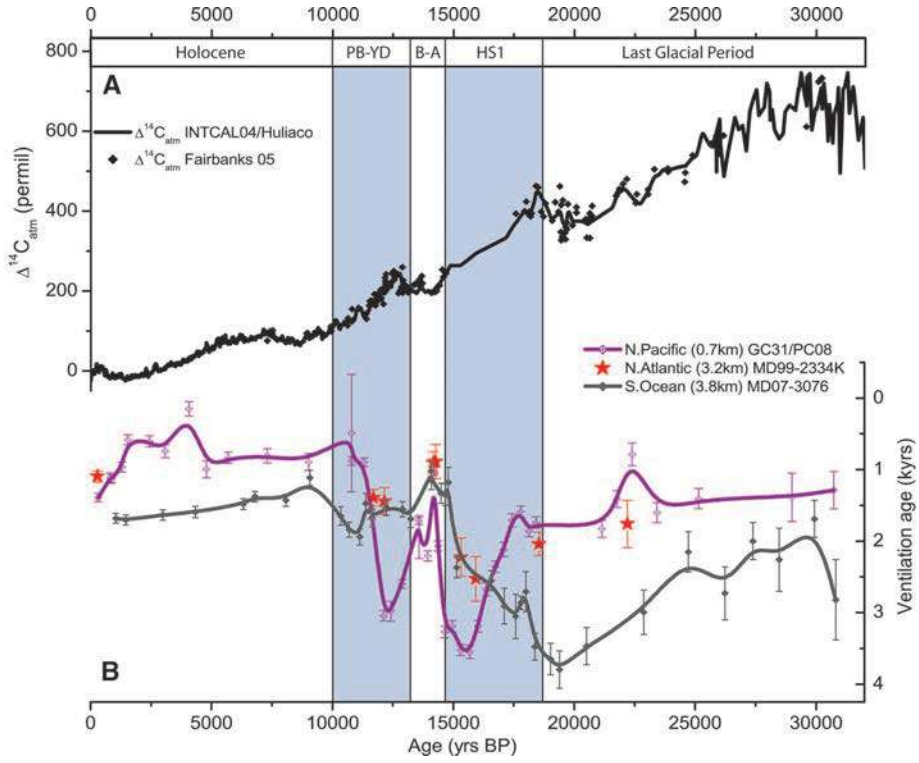


**Fig. 3.** Atmospheric $\Delta^{14}C$ change and deep-water reservoir age variability in the shallow Pacific, deep North Atlantic (*13*, *15*), and the deep Southern Ocean (this study). (**A**) Atmospheric $\Delta^{14}C$ [black diamonds, coral data (*22*); black line, INTCAL04 calibration curve (*23*) spliced with the Cariaco data set from 26 ky B.P. (*7*)]. (**B**) Deep water reservoir ages, derived from the offset between benthic- and atmospheric-$^{14}C$ ages (reversed *y* axis). Solid red stars indicate MD99-2334K from the deep Northeast Atlantic (*13*), purple crossed diamonds and b-spline smoothed line indicate GCMV99-GC31/PC08 from the shallow Pacific (*11*), and gray diamonds and b-spline smoothed indicate MD07-3076 from the Southern Ocean (this study). Error ranges for MD99-2334K and MD07-3076 indicate combined planktic and benthic $^{14}C$ age uncertainties (1σ), whereas those for GCMV99-GC31/PC08 are 2σ uncertainties in benthic $^{14}C$ ages alone (Fig. 2E). Shaded vertical bars highlight the coincidence of rapid changes in deep water ventilation with marked changes in $\Delta^{14}C_{atm}$ and major North Atlantic chronozones.

One important question that arises concerns the extent to which the changes in deep-water ventilation recorded in MD07-3076 help to explain the apparent glacial $\Delta^{14}C_{atm}$ excess and the rapid 190 per mil (‰) drop in $\Delta^{14}C_{atm}$ during HS1 (*8*) (Fig. 1). Answering this question accurately would require knowledge of the exact volume of deep water that was affected by the ventilation changes recorded at the site of MD07-3076. Without this knowledge, we can only say that if the ~2000-year reduction in B-Atm recorded across HS1 in MD07-3076 (Fig. 2E) was experienced by ~30% of the ocean [all water deeper than the next deepest $^{14}C$ constraint from the glacial Pacific (*12*)], this could explain just over half of the 190‰ drop in atmospheric $\Delta^{14}C$ across the mystery interval (*15*). At the very least, this provides cause for optimism regarding the eventual reconciliation of the deglacial "radiocarbon mystery" (*8*), though it also underlines the need for a wider array of deep-ocean $^{14}C$ data with precise calendar chronologies.

The cause of the transient increase in ventilation recorded during the ACR/Bølling-Allerød in MD07-3076 [and in other records from the Atlantic and Pacific (Fig. 3B)] is also difficult to assess accurately without knowledge of the changing "end-member" composition and mixing ratio of local deep water. Neodymium isotope data from core RC11-83 in the deep Cape Basin (*16*) suggests a variable but generally increased influence of northern-sourced deep water during the ACR/Bølling-Allerød relative to the LGM, but crucially not relative to the late Holocene. If this record is taken as representative of end-member mixing ratio changes at our more open Atlantic site, it follows that mixing ratio changes alone might

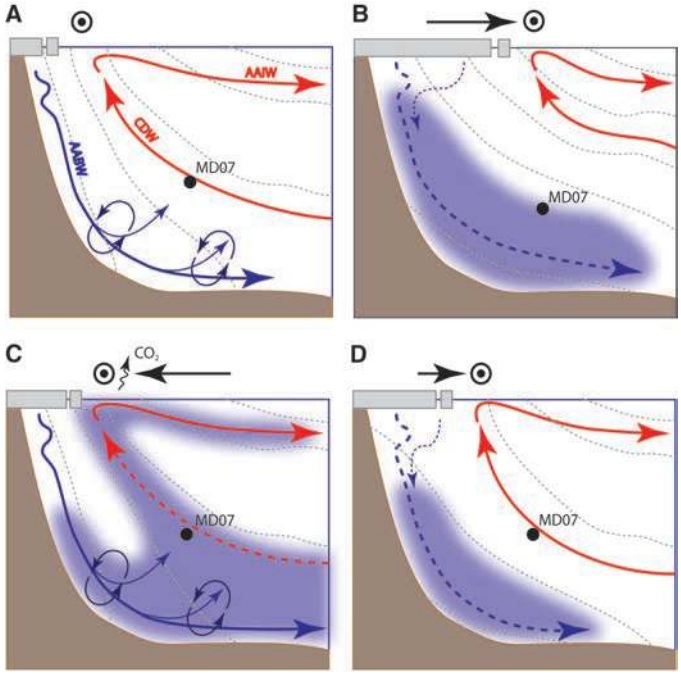


**Fig. 4.** Schematic illustration of hypothesized changes in Southern Ocean overturning across the last deglaciation (with south at left). (**A**) The modern overturning. Red arrows indicate the "upper overturning limb," which here includes CDW upwelling in the Southern Ocean at the ACC divergence and AAIW flowing northwards at shallow depths. Upper and lower CDW, which may include North Atlantic– and Antarctic-sourced water in variable proportions, have been combined for simplicity. Blue arrows indicate the "lower overturning limb," which consists of Antarctic Bottom Water (AABW) and its derivatives. Gray dashed lines indicate hypothetical isopycnals. Dark blue circular arrows indicate intense diapycnal mixing around topography in the Southern Ocean, which permits effective lower-limb overturning and the incorporation of AABW into CDW (*15*). Sea ice is represented by the gray boxes (top left), and the westerly wind position is indicated by the dotted circle (top). The solid circle marks the approximate position of core MD07-3076. (**B**) LGM overturning. The North Atlantic (salt) contribution to the upper-limb circulation is subdued relative to the present; Antarctic sea ice and the effective westerly wind stress in the Southern Ocean (driving isopycnal outcropping) are pushed far northward (black arrow). Flattened and widely spaced isopycnals south of the main outcropping area cause the $^{14}C$-depleted lower overturning limb to expand without substantial diapcynal mixing into CDW. The shaded area indicates a $^{14}C$-depleted, high potential $Pco_2$ deep-water mass. (**C**) HS1/YD overturning. The supply of North Atlantic deep water to CDW is severely reduced, the Southern Ocean warms in part because of the bipolar seesaw, Antarctic sea ice retracts substantially from its maximum glacial extent, and the main isopycnal outcrop area shifts southward. Poorly ventilated (high potential $Pco_2$) AABW is drawn upward along steepened isopycnals and mixed to a greater extent into CDW, which releases $^{14}C$-depleted $CO_2$ to the atmosphere when brought to the surface. (**D**) Bølling-Allerød overturning. The Southern Ocean cools because of the bipolar seesaw, and sea ice reverses its retreat. Mixing of AABW into upward-flowing CDW is impeded once again, and the release of $^{14}C$-depleted $CO_2$ pauses as a result.

not account for near modern deep-water ventilation ages observed during the ACR/Bølling-Allerød (Fig. 2E). This would suggest that either the export rate or ocean-atmosphere equilibration of one or both of the main Atlantic deep-water end-members (North Atlantic and/or Antarctic) increased during the ACR/Bølling-Allerød.

Our results demonstrate the existence before HS1 of an exceptionally aged abyssal carbon reservoir that could have substantially contributed to the sequestration of $CO_2$ in the deep sea during the last glacial period. These results also underline the potential importance of the combined effects of changing Antarctic sea ice, wind forcing, and abyssal stratification on the deglacial rise of $CO_2$. As illustrated schematically in Fig. 4, we envisage that although the meridional extent of Antarctic sea ice should influence the efficacy of the westerly wind stress that can effectively be applied to the Antarctic Circumpolar Current (ACC) to drive the upwelling of the densest classes of CDW in the Southern Ocean, the impact of upwelling on atmospheric $CO_2$ ($\Delta^{14}C_{atm}$ and $\partial^{13}CO_2$) might ultimately be determined by changes in the potential $P_{CO_2}$ and sequestration age of the CDW that is brought to the surface. Thus, the deglacial trends in atmospheric $CO_2$, $\partial^{13}CO_2$, and $\Delta^{14}C_{atm}$ may have been interrupted during the ACR/Bølling-Allerød at least partly as a result of a pronounced increase in the ventilation of CDW brought to the surface Southern Ocean at this time (Figs. 2D and 4D). In contrast, with the preponderance of exceptionally aged CDW during HS1 and the YD [and with Antarctic sea ice already pulled back from its maximal meridional extent (Fig. 4C)], high potential $P_{CO_2}$ water would be brought to the surface Southern Ocean instead. The result would have been to greatly enhance the release of $^{14}C$-depleted $CO_2$ to the atmosphere, as well as the export of $^{14}C$-depleted water from the ACC to the Atlantic and Pacific at these times.

### References and Notes


1. W. Broecker, G. M. Henderson, *Paleoceanography* **13**, 352 (1998).
2. R. F. Anderson *et al*., *Science* **323**, 1443 (2009).
3. S. Barker *et al*., *Nature* **457**, 1097 (2009).
4. U. Siegenthaler *et al*., *Science* **310**, 1313 (2005).
5. J. Ahn, E. J. Brook, *Science* **322**, 83 (2008).
6. F. Primeau, *J. Phys. Oceanogr.* **35**, 545 (2005).
7. K. Hughen, J. Southon, S. Lehman, C. Bertrand, J. Turnbull, *Quat. Sci. Rev.* **25**, 3216 (2006).
8. W. Broecker, S. Barker, *Earth Planet. Sci. Lett.* **256**, 90 (2007).
9. L. F. Robinson *et al*., *Science* **310**, 1469 (2005).
10. E. Monnin *et al*., *Science* **291**, 112 (2001).
11. T. M. Marchitto, S. J. Lehman, J. D. Ortiz, J. Flückiger, A. van Geen, *Science* **316**, 1456 (2007).
12. W. Broecker, E. Clark, S. Barker, *Earth Planet. Sci. Lett.* **274**, 322 (2008).
13. L. C. Skinner, N. J. Shackleton, *Paleoceanography* **19**, PA2005 (2004).
14. E. D. Galbraith *et al*., *Nature* **449**, 890 (2007).
15. Materials and methods are available as supporting material on *Science* Online.
16. A. M. Piotrowski, S. L. Goldstein, S. R. Hemming, R. G. Fairbanks, *Earth Planet. Sci. Lett.* **225**, 205 (2004).
17. A. C. Parnell, J. Haslett, J. R. M. Allen, C. E. Buck, B. Huntley, *Quat. Sci. Rev.* **27**, 1872 (2008).
18. H. J. Smith, H. Fischer, M. Wahlen, D. Mastroianni, B. Deck, *Nature* **400**, 248 (1999).
19. H. J. Spero, D. W. Lea, *Science* **296**, 522 (2002).
20. L. Pena, I. Cacho, P. Ferretti, M. A. Hall, *Paleoceanography* **23**, PA3101 (2008).
21. P. Kohler, H. Fischer, G. Munhoven, R. E. Zeebe, *Global Biogeochem. Cycles* **19**, GB4020 (2005).
22. R. G. Fairbanks *et al*., *Quat. Sci. Rev.* **24**, 1781 (2005).
23. P. J. Reimer *et al*., *Radiocarbon* **46**, 1029 (2004).
24. P. Kohler, R. Muscheler, H. Fischer, *Geochem. Geophys. Geosyst.* **7**, Q11N06 (2006).
25. R. Muscheler, J. Beer, P. W. Kubik, H.-A. Synal, *Quat. Sci. Rev.* **24**, 1849 (2005).
26. C. Laj, C. Kissel, J. Beer, in *Timescales of the Paleomagnetic Field*. (American Geophysical Union, 2004), vol. 145, pp. 255–265.
27. A. Indermuhle, E. Monnin, B. Stauffer, T. F. Stocker, M. Wahlen, *Geophys. Res. Lett.* **27**, 735 (2000).
28. B. Lemieux-Dudon *et al*., *Quat. Sci. Rev.* **29**, 8 (2010).
29. H. Fischer *et al*., *Earth Planet. Sci. Lett.* **260**, 340 (2007).


30. We are grateful to N. Caillon, F. Dewilde, G. Isguder, H. Rebaubier, L. Booth, P. Ljubic, and K. James for technical assistance. A. Parnell provided generous and invaluable help with *Bchron*, and P. Köhler very kindly provided unpublished $\Delta^{14}C_{atm}$ simulations. We thank R. Gersonde and A. Mackensen for sharing their South Atlantic expertise, and we acknowledge the crew of the R/V Marion Dufresne and the Paul Emile Victor Institute (IPEV) who collected core MD07-3076CQ. This work was funded by the Royal Society, by Natural Environment Research Council Radiocarbon grant 1245.1007, and via a University Fellowship held by L.C.S. This work was facilitated by a visiting fellowship held by L.C.S. at ANU and by travel grants from the Royal Society and Christ's College. C.W. and E.M. are supported financially by Centre National de la Recherche Scientifique, Institut National des Sciences de l'Univers, and Commissariat à l'Energie Atomique. This is Laboratoire des Sciences du Climat et l'Environnement contribution 4188.

Supporting Online Material for

# Ventilation of the deep Southern Ocean and deglacial $CO_2$ rise

L.C. Skinner[1]*, S. Fallon[2], C. Waelbroeck[3], E. Michel[3], S. Barker[4]

[1] Godwin Laboratory for Palaeoclimate Research, Department of Earth Sciences, University of Cambridge, Downing Street, Cambridge, CB2 3EQ, United Kingdom

[2] Research School of Earth Sciences, Australian National University, Canberra, ACT 0200, Australia

[3] LCSE/IPSL, Laboratoire CNRS-CEA-UVSQ, Bat. 12, Avenue de la Terrasse, F-91198, Gif-sur-Yvette CEDEX, France

[4] School of Earth and Ocean Sciences, Cardiff University, Cardiff CF10 3YE, United Kingdom

* Author to whom correspondence should be addressed (email: luke00@esc.cam.ac.uk)

**This PDF file includes**

## Materials and Methods

Core MD07-3076 (44° 4.46'S; 14°12.47'W, 3,770m) was recovered from the eastern flank of the mid-Atlantic ridge, in the Atlantic sector of the Southern Ocean. Currently, the core site is bathed in a predominantly southward flowing mixture of modified North Atlantic Deep Water (NADW) and Lower Circumpolar Deep Water (LCDW), which eventually feeds into the core of eastward flowing Circumpolar Deep Water (CDW) (*1*) (Fig. S1). Downstream of the core site, CDW is further modified by incorporation of UCDW (from above) and AABW (from below) and subsequently exported into the deep Pacific and Indian basins, where its NADW component currently helps to bolster their respective salt and radiocarbon budgets (*2, 3*). Internal mixing of LCDW upward into UCDW and subsequently the conversion of UCDW into sub-thermocline water (especially in the southwest Atlantic- and southeast Pacific sectors of the Southern Ocean) allows water flowing past the site of MD07-3076 to also find its way into Antarctic Intermediate Water (AAIW). Indeed, a recent analysis (*4*) of Lagrangian flow paths in a simulation of the global circulation indicates that of the 14.1Sv of LCDW that enters the Southern Ocean in the Atlantic sector, roughly 78% leaves the Southern Ocean again in the lower limb of circulation (as LCDW and bottom water, BW), while ~13% leaves in the upper limb of circulation (as mode and thermocline water).

Surface-water above the core location is currently situated between the sub-tropical and sub-polar fronts (Fig. S1). In this hydrographic context, the planktonic foraminifer species *Globigerina bulloides* and *Neogloboquadrina pachyderma* (left-coiling) are near-surface dwellers (0-300m), with warmer (and eutrophic) and colder habitat affinities respectively. The deep-dwelling species *Globorotalia inflata* maintains a consistent shallow sub-surface habitat (50-300m) (*5*).

***Radiocarbon dating***

Samples of planktonic foraminifera (monospecific) and of benthic foraminifera (mixed species) were picked from the >212μm fraction of core MD07-3076. Samples were always larger than 5 mg carbonate. All samples were crushed between glass plates, transferred to plastic lock-cap vials and cleaned according to a protocol similar to that developed for Mg/Ca analysis (*6*). Clays and particulate carbonate material were removed by repeated rinses in deionised water, followed by oxidation of organic matter in 2% $H_2O_2$ (buffered by NaOH) maintained at 90°C. Following a weak acid leach and a final set of rinses in deionised water, the samples were transferred to glass vials for drying and graphitisation. The majority of samples were graphitised at the Australian National University Research School of Earth Sciences geochronology unit using the hydrogen and iron catalyst method, and subsequently analysed using a National Electrostatic Corporation (NEC) Single Stage Accelerator Mass Spectrometer (SSAMS), usually with online $\delta^{13}C$ measurement (see Table S1). A subset of the samples (11) was graphitised and analysed at the SUERC/NERC Radiocarbon Facility (see Tables 1 and 2). A number of inexplicable 'flyers' amongst the planktonic dates (*G.inflata* in particular) were rejected due to obvious contamination by up to 25% modern carbon. We believe that this contamination may represent the precipitation of carbonate phases from modern seawater soon after core-recovery. The retained conventional ($\delta^{13}C$-normalised) radiocarbon ages from MD07-3076 are illustrated in Fig S2 and are summarised in Tables S1 and S2.

Three additional benthic radiocarbon dates were obtained from core MD99-2334K (*S7*) according to the same methodology. These dates (also $\delta^{13}C$-normalised) are summarised in Table S3.

***Planktonic Mg/Ca***

Mg/Ca was measured on samples of 30 specimens of *G. bulloides* and of 40 specimens of *N. pachyderma*, cleaned following the method described by Barker

and colleagues (*S6*) to eliminate contamination from clays and organic matter. Analyses were performed on a Varian Vista Pro Inductively Coupled Plasma Optical Emission Spectrometer (ICP-OES) following the procedure of (S*8*). Precision for measured Mg/Ca ratios determined from replicate runs of a standard solution of Mg/Ca = 5.23 mmol/mol is 0.4% (relative standard deviation, RSD) (S*9*). Precision for *N.pachyderma* and *G.bulloides* samples is respectively 8.1 and 4.9% (pooled RSD). Note that the uncertainty on *N.pachyderma* Mg/Ca measurements increases for small samples with very low measured Ca concentrations over the last deglaciation.

Derivation of SST from Mg/Ca ratio can be biased if foraminiferal shells have undergone partial dissolution (e.g. *S10*). Here, a significant control on measured Mg/Ca patterns due to dissolution is ruled out on the basis of a lack of significant correlation between Mg/Ca and shell weights, or between Mg/Ca and shell fragmentation counts. Absence of silicate contamination was controlled by measuring Fe, Al and Mn content, with a maximum allowed Fe/Mg ratio of 0.1 mol.mol-1 for high Mg/Ca samples. Plotting Mg/Ca against Al/Ca (or Fe/Ca) does not show any outlier that would indicate detrital contamination. Maximum contribution of Mg from Mn-Fe-oxide is about 1% (given the Mg/Mn ratio of about 0.1 mol/mol in nodules and micro nodules (see S*6* and references therein)).

Mg/Ca values of *G.bulloides* (0 – 104 cm depth) and *N.pachyderma* (84 – 400 cm depth) were converted into SST following the calibration for the South Atlantic of (*S11*) and of (*S12*), respectively. Mg/Ca-reconstructed core-top SST values from *G.bulloides* correspond well with present summer temperature (January, February, March) from the site (10.1°C, WOA05), as well as with summer Modern Analogue Technique (MAT) temperature reconstructions (*S13*) based on foraminiferal abundances in core MD07-3076. SSTs reconstructed from *N.pachyderma* (from glacial and late-glacial intervals) fall within the seasonal range suggested by MAT temperature reconstructions in MD07-3076, and agree

with temperatures inferred from a regression of SST *versus* percentages of *N.pachyderma* (left-coiling) (*S14*).

***Chronology and surface reservoir age constraints***

The age-scale for the $CO_2$ data shown in Fig. 1 and Fig. 2 in the text has been derived by B. Lemieux and co-workers based on alignment of methane variability in the NGRIP and EDC ice-cores combined with gas-age versus ice-age modelling (*S15*). This age-scale is consistent with the GICC05 gas- and ice age-scales, and shifts the $CO_2$ record toward slightly older ages relative to the original EDC1 age-scale of (*S16*), in particular across HS1. In order to place $\partial^{13}CO_2$ data from Taylor Dome (*S17*) on a consistent age-scale, methane variability in this ice-core has been aligned to methane variability in the NGRIP and EDC ice-cores, again placed on the NGRIP-GICC05 gas age-scale.

For marine cores, a common approach for generating chronologies is to assume a constant surface-water reservoir age in order to generate a 'calibrated radiocarbon' (calendar) age-scale based on planktonic radiocarbon dates. An alternative approach is to use a stratigraphically constrained calendar age-scale in order to determine changes in surface- and deep-water $\Delta^{14}C$ (e.g. *S7*), or (in the absence of planktonic dates) of $\Delta^{14}C_{dw}$ only (e.g. *S18*). Indeed, at high latitudes and in regions of variable and potentially strong upwelling or air-sea disequilibrium (such as at the site of MD07-3076), the assumption of constant surface reservoir ages will be unwarranted, necessitating the latter approach. Accordingly, we assess the degree of surface-reservoir age variability at the site of MD07-3076 by reference to two independent sets of chronostratigraphic (calendar) age constraints.

The first set of calendar age constraints is obtained via the correlation of regional temperature trends recorded in the Antarctic ice-cores and recorded in the *G.bulloides* and *N.pachyderma* Mg/Ca records from MD07-3076 (Fig. S3). The most important and robust tie-points available are the early Holocene thermal

maximum, the Antarctic Cold Reversal (ACR), the mid-point of the primary deglacial warming, and the cold interval between AIM 2 and AIM3 (only ages younger than ~30 ka BP are relevant for our radiocarbon results). We adopt the most recent ice-core chronology for the EDML, EDC and NGRIP ice-cores noted above (*S15*). This chronology has been produced using inverse methods, taking into account both glaciological modelling and gas/ice stratigraphic constraints, so as to yield simultaneous and consistent dating of Antarctic and Greenland ice-cores with quantifiable uncertainties. We use the highest resolution EDML ice-core for the purposes of correlation, though in principle any other chronostratigraphically aligned ice-core (e.g. EDC) may be used instead.

As illustrated in Fig S4A, each of the available chronostratigraphic tie-points that link MD07-3076 to the EDML ice-core implies a calendar age range that is defined by a combination of the 'absolute' uncertainty in the ice-core chronology and the correlation uncertainty that arises from the ~200 year average sampling resolution in the marine core. For the least certain of the tie-points (the onset of warming across the deglaciation) we apply an additional *ad hoc* uncertainty of 500 years. The ice-core calendar age-ranges obtained in this way imply a range of possible planktonic reservoir ages at each chronostratigraphic tie-point. We calculate these as the difference between the measured planktonic radiocarbon age at each tie-point and the radiocarbon ages predicted for each ice-core calendar age range by the IntCal04 (*S19*) and Cariaco Basin (*S20*) radiocarbon calibration datasets. The resulting ice-core derived reservoir age estimates are shown in Fig S4B (filled stars), along with the estimated uncertainty range that can be supported by ice-core chronology and correlation errors (shaded area). This approach suggests the occurrence of two main periods in the past when surface reservoir ages deviated significantly from the modern value of ~700 years (*S21*).

In order to obtain a second independent assessment of past surface reservoir age variability, we compare radiocarbon dates from MD07-3076 and from core

TNO57-21 (*S22*). The cores are aligned based on a correlation of Mg/Ca-based sub-polar surface-water temperature reconstructions at each location (Fig. S5). The Mg/Ca record from TNO57-21 (4,981m water depth) was shown by (*S22*) to have been affected by partial dissolution across the HS1 interval (~15-17 ka BP), and was adjusted accordingly. Here we use the unadjusted data, on the basis of their similarity to the Mg/Ca record from core MD07-3076, which has not been severely affected by dissolution (shell weights do not correlate with Mg/Ca and peak foraminifer fragmentation counts in MD07-3076 never reach even the lowest levels observed in TNO57-21). However, using the 'dissolution adjusted' Mg/Ca record from TNO57-21 instead makes little difference to the alignment of the cores, since the rapid changes at ~17.7 and 14.5 ka BP bracket the interval of inferred dissolution.

By calculating planktonic $^{14}C$ age-offsets for correlative events in cores MD07-3076 and TNO57-21 (interpolated $^{14}C$ ages in TNO57-21 must be used to do this), the relative magnitude of surface reservoir ages at the two core sites can then be inferred. This is illustrated in Fig S6A, where it can be seen that radiocarbon ages in MD07-3076 deviate from those of TO57-21 by a large margin, up to 2,500 years (too large to be explainable by correlation uncertainties for example). On the strength of the TNO57-21 age-scale and the implied constant 600 year reservoir age at that site (*S22*), reservoir-age variability can thus be inferred for MD07-3076 (Fig S6B). In order to take into account uncertainties in the reservoir ages obtained in this way we apply a maximum error of 600 years (i.e. 100% of the reservoir age applied in core TNO57-21). This uncertainty estimate provides a very strong lower bound on the inferred reservoir ages shown in Fig S6B, since it excludes the possibility of reservoir ages dropping below zero at the site of TNO57-21, which is impossible.

As shown in Fig S6B, the alignment with TNO57-21 yields strikingly similar reservoir age estimates (open circles, Fig S6B) to those derived from the ice-core alignment (red stars, Fig S6B). Where ice-core and marine core constraints on

the reservoir ages overlap they deviate by significantly less than the estimated uncertainty in the reservoir age estimates (suggesting that the uncertainty in our reservoir ages may be less than estimated). Because of the strong coherence between the two sets of chronostratigraphic constraints, and because they clearly demonstrate that the assumption of constant reservoir ages is not warranted in the absence of evidence to the contrary, we make use of all of the available chronostratigraphic constraints in order to derive a 'best estimate' of past reservoir age variability at the site of MD07-3076. Our approach is to apply a constant modern reservoir age of 700 years except where our reservoir age estimates indicate a change that exceeds the associated uncertainty limits.

Fig S7 summarises the reservoir age constraints described above, as well the best estimate reservoir age scenario that is applied to core MD07-3076 and two alternative bounding (maximum and minimum) reservoir age scenarios. Because reservoir age biases (errors) must correlate with chronology biases (e.g. larger reservoir ages imply a younger chronology), it is necessary to derive a different chronology for each of the bounding reservoir age scenarios. We derive these chronologies using the Bayesian radiocarbon calibration and sediment-age modelling framework of *Bchron* (*S23*). The statistical treatment of *Bchron* takes into account the high density of reservoir-corrected planktonic radiocarbon age-constraints available, as well as the calibration uncertainty in the radiocarbon dates, in order to provide a quantitative estimate of the uncertainty in the resulting age-model. Here, the uncertainty range in our best estimate chronology is on average ±224 years back to 34 ka BP (the lowest uncertainties apply to the top of the core where the dating resolution highest, see Fig S8). Note that the uncertainty range in the chronology is not symmetrical or normally distributed. For simplicity we therefore express the uncertainty range here (and in Tables S1 and S2) as half of the difference between the 2.5% and 97.5% HDR.

The uncertainty range produced by the statistical treatment of *Bchron* is distinct from the possible bias in the age-scale that would arise from having over/under

estimated surface reservoir ages (see below). It is also important to note that biases in surface-water reservoir age correction will not affect the shape of the benthic-planktonic $^{14}$C-age offset reconstruction (Fig 2D of the manuscript). Hypothetically, if surface reservoir ages have been significantly underestimated, then inferred deep-water apparent ventilation ages (relative to the atmosphere, B-Atm) should be increased and the chronology shifted to younger ages (and vice versa). However, the marine and ice-core chronostratigraphic constraints discussed above do not support the existence of such biases. This is summarised in Fig S8, which shows a very good agreement between our 'best estimate' (radiocarbon-based) *Bchron* sediment age-model, and both the TNO57-21 age-scale of (*S22*) and the most recent Antarctic ice-core chronology.

***Uncertainties in ventilation age reconstruction***

Apparent ventilation ages are calculated here as the difference between benthic and planktonic radiocarbon ages (B-P), plus the surface reservoir age (R). Three distinct types of uncertainty therefore apply to our apparent ventilation age (B-Atm = B-P+R) reconstruction: 1) random uncertainties in B and P due to the radiocarbon dating procedure; 2) possible biases in R due to reservoir age over/under estimation; and 3) random uncertainties in age-depth modelling, arising from calibration and sediment accumulation rate interpolation uncertainties. We illustrate these uncertainties separately (e.g. Fig 2 of the manuscript and Fig S8) in order to emphasise their different sources and associations.

The first type of uncertainty is shown by vertical error bars in Fig 2D and 2E of the manuscript, and amounts to the sum of the benthic and planktonic 1$\sigma$ dating uncertainties. The second type of uncertainty (discussed in the preceding section) represents a bias in the magnitude of R, and correlates negatively with chronology biases (Table S2). The precise magnitude of these chronology biases depends on the radiocarbon calibration and sediment age-depth interpolation procedure, and its uncertainty is defined in the same way as the

random chronology uncertainty (the third type of uncertainty listed above). In order to estimate this third type of uncertainty, we use the Bayesian statistical treatment of *Bchron* (*S23*). While the uncertainty in B-P tells us how precise our radiocarbon dating is, the uncertainty in R tells us how tight the chronostratigraphic framework for MD07-3076 is. It is useful to distinguish this uncertainty from the *Bchron* age-modelling uncertainty, which instead tells us how precisely we can constrain accumulation rate variability down-core, based primarily on the dating resolution in MD07-3076. Thus, for example, the statistical treatment of *Bchron* tells us that by using a very large number of planktonic radiocarbon dates we are able to constrain down-core changes in sediment accumulation rate very well. On the other hand, the estimated possible range in R tells us how the absolute magnitude of accumulation rates (and also B-Atm) might change if we were to adopt an alternative chronostratigraphic framework (i.e. larger or smaller R values). It is important to note that exploiting the maximum/minimum limits of the uncertainty in R at or near stratigraphic tie-points between MD07-3076 and the Antarctic ice-cores must imply significant biases in the correlation procedure (Figs S3 and S4) or in the published ice-core chronology.

***Past deep-water and atmospheric radiocarbon budgets***

In order to assess the degree to which the deglacial change in the radiocarbon-age of deep-water recorded in MD07-3076 might account for the rapid 190 ‰ drop in atmospheric $\Delta^{14}C$ across the so-called 'mystery interval' (*S24*) a simple mass-balance calculation may be performed. Here we consider an atmosphere in communication with a four-box ocean that consists of: 1) a surface slab 0-200m (~5% of the ocean volume); 2) an upper ocean box 200-1,750m (~30%); 3) an intermediate box 1,750-3,000m (~30%); and 4) a deep box extending below ~3,000m (~35%). We can allocate carbon inventories to each of these boxes, based on expected carbon concentrations and approximate box volumes (as predicted by the hypsometry of the sea floor in the case of the ocean boxes). Given the total radiocarbon budget, and the radiocarbon budgets of any four of

the reservoirs in this model, the radiocarbon activity of the fifth box can be calculated. If we maintain the apparent ventilation age (reservoir age) of the surface ocean box at 500 yrs and that of the upper- and intermediate ocean boxes at 2,000 yrs (*S24*), while changing the reservoir age relative to the atmosphere of the deepest ocean box by 2,000 years (i.e. the B-Atm change recorded in MD07-3076 at 3,770m)), then the atmospheric radiocarbon activity drops by just over 100‰, which is ~60% of the entire 'mystery interval' drop. If we consider instead the 1,250 year change in B-P recorded in MD07-3076 between the glacial and the Bølling-Allerød, then ~35% of the mystery interval drop is explained. These calculations use standard values for the total volume of the atmosphere ($1.773 \times 10^{20}$ mol) and the ocean ($1.3 \times 10^{18}$ $m^3$), the radiocarbon half-life (5568 yr), and the global carbon budget (35832 Gt).

We can also calculate using this simple model that the full 190‰ drop, if not accounted for at all by changes in radiocarbon production, could hypothetically be explained by relatively small changes in the mean ventilation age of the whole upper ocean (e.g. ~100 yrs over 60% of the ocean – too small to identify using B-P radiocarbon offsets) combined with a slightly larger change in the mean ventilation of the deepest ocean box (e.g. ~ 3,000 yrs on *average,* over 35% of the ocean). In the latter hypothetical case, the results from MD07-3076 could be representative of the ventilation change experienced by a better-ventilated 'fringe' of the abyssal carbon reservoir, which in turn would have to have been >>3,000 years old relative to the atmosphere. In any event, the results from MD07-3076 might explain over half of the mystery interval $\Delta^{14}C_{atm}$ drop.

**Figure S1.**

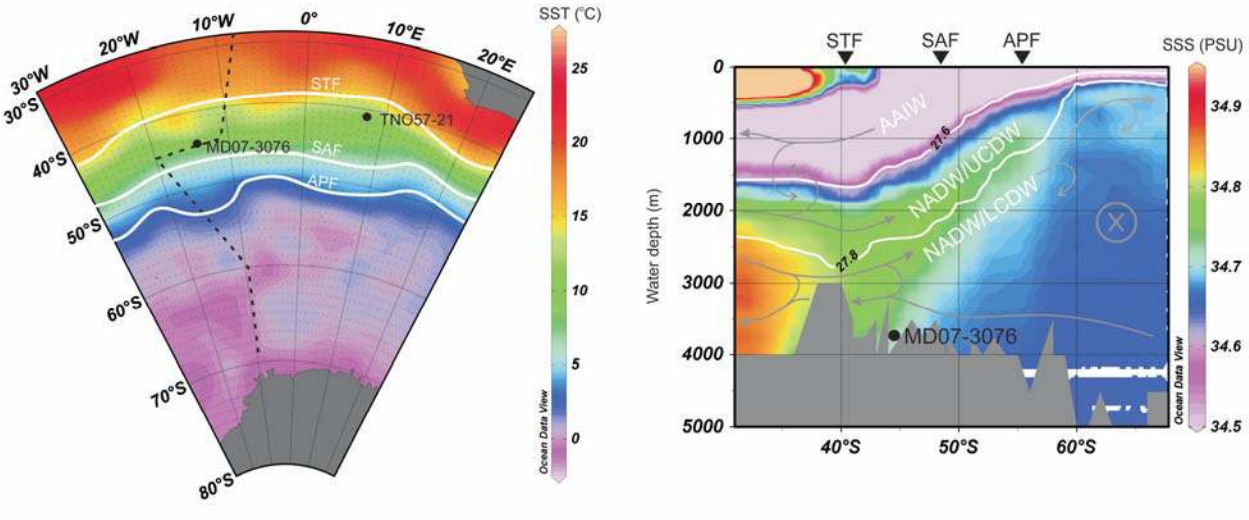


**Figure S1.** Location map and hydrography for MD07-3076 CQ (44° 4.46'S; 14°12.47'W, 3,770m). **(A)** Location of MD07-3076 CQ in the context of average annual sea surface temperatures (*S26*), with the approximate positions of the sub-tropical front (STF), the Sub-Antarctic Front (SAF) and the Antarctic Polar Front (APF) shown by white lines (*S27*). The grey dotted line indicates the position of the section shown opposite in B. Also shown is the position of TNO57-21 (41° 6'S; 7°48'E, 4,981m) (*S22*), which is also referred to in the text. **(B)** Salinity section, showing the position of core MD07-3076 (black circle), the approximate positions of the subtropical front (STF), the sub-Antarctic front (SAF) and the Antarctic Polar Front (APF), as well as the 27.6 $kgm^{-3}$ and the 27.8 $kgm^{-3}$ potential density isopleths (thick white lines), which approximately define the divisions between: 1) Antarctic Intermediate Water (AAIW) and the underlying salty mixture of North Atlantic Deep Water (NADW) and Upper Circumpolar Deep Water (UCDW); and 2) the NADW/UCDW salinity maximum and the underlying mixture of NADW and Lower Circumpolar Deep Water (LCDW) (S*28*). Grey arrows give an impression of the prevailing direction of water flow, and of the modification of AAIW, NADW/UCDW and NADW/LCDW properties via vertical mixing of these water-masses (*S1*). At the longitude and latitude of MD07-3076, NADW/LCDW currently incorporates water from above (~1 Sv) and below (~5 Sv) via diapycnal mixing, with a net contribution of ~12 Sv to the eastward flow of the Antarctic Circumpolar Current (*S1*). The crossed circle indicates flow into the plane of the section, toward the Indo-Pacific basins.

**Figure S2.**

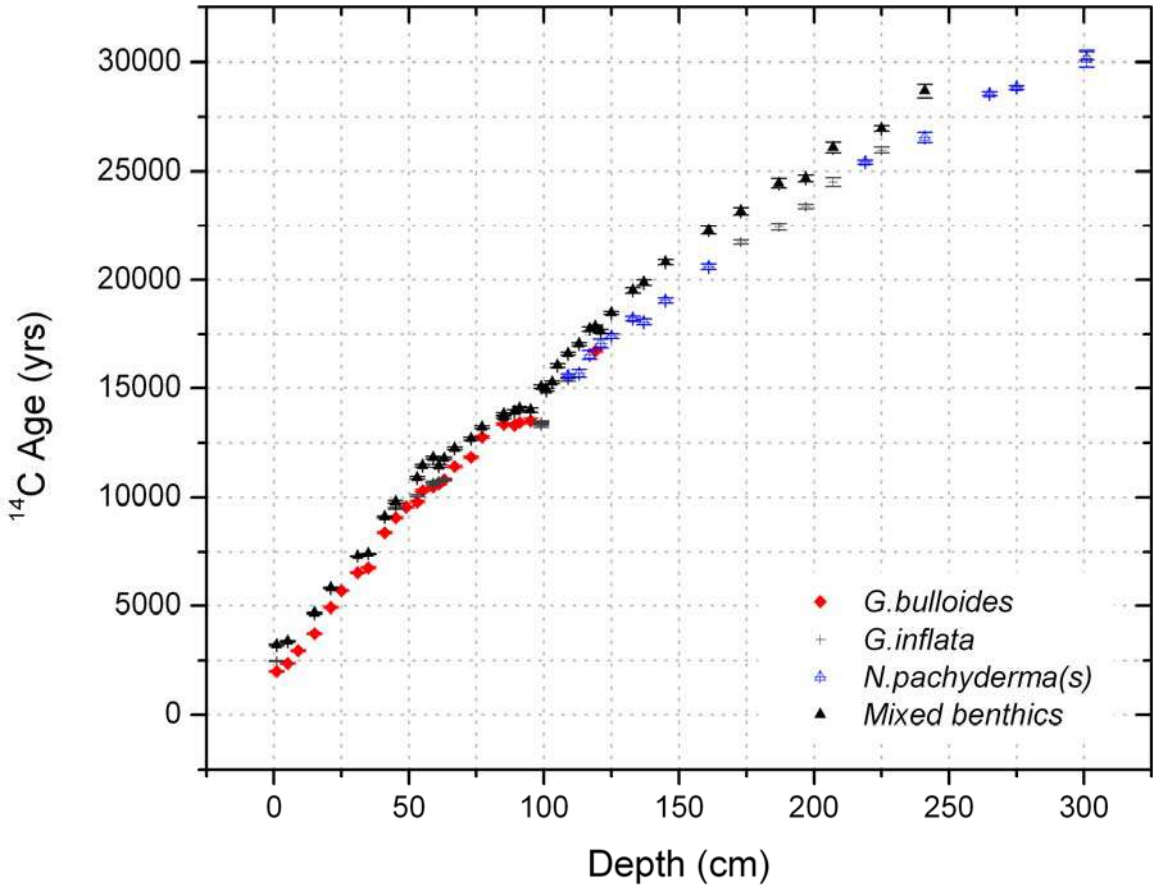


**Figure S2.** Summary of raw MD07-3076 radiocarbon ages ($\delta^{13}$C-normalised, but without reservoir age correction and uncalibrated to calendar years), with associated 1$\sigma$-uncertainties.

**Figure S3.**

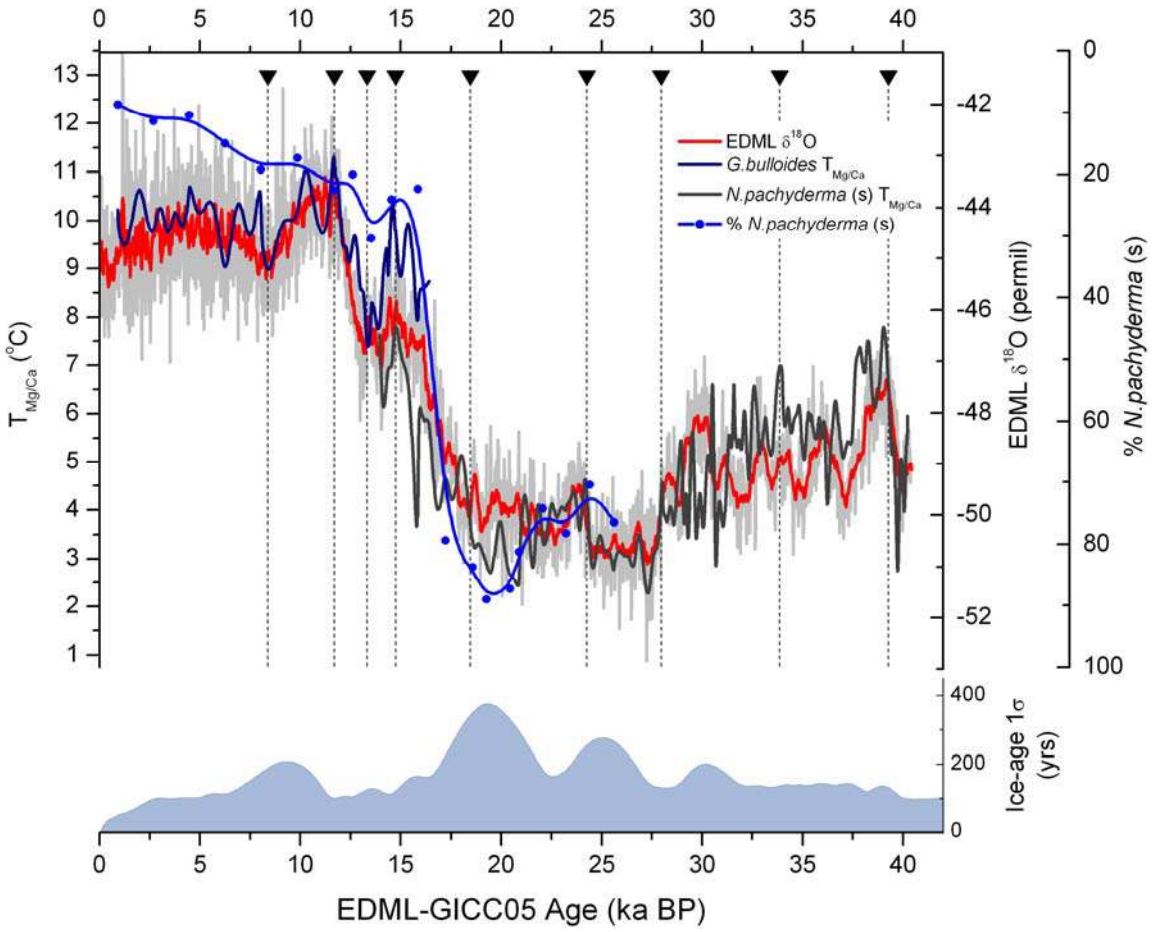


**Figure S3.** Derivation of a calendar age-scale for MD07-3076 via correlation of Antarctic temperature changes recorded in the EDML ice-core (*S15*) (light grey line with 5-point smoothed heavy red line) with sea-surface temperature changes, reconstructed from Mg/Ca ratios in *G.bulloides* (navy blue line) and *N.pachyderma* (dark grey line) from core MD07-3076. Tie points are indicated by black inverted triangles and dashed vertical lines. The tie point at ~33.2 ka BP is used only to provide a rough ice-core age-estimate for the deepest $^{14}$C-dated levels in MD07-3076 (see Fig S4). Confirmation of the correct positioning of the Termination in the overlapping Mg/Ca records is provided by counts of the polar foraminifer species *N.pachyderma* (blue dots with b-spline smoothed blue line). The lower panel shows the 1$\sigma$ uncertainty in the EDML ice-core chronology (*S15*).

**Figure S4.**

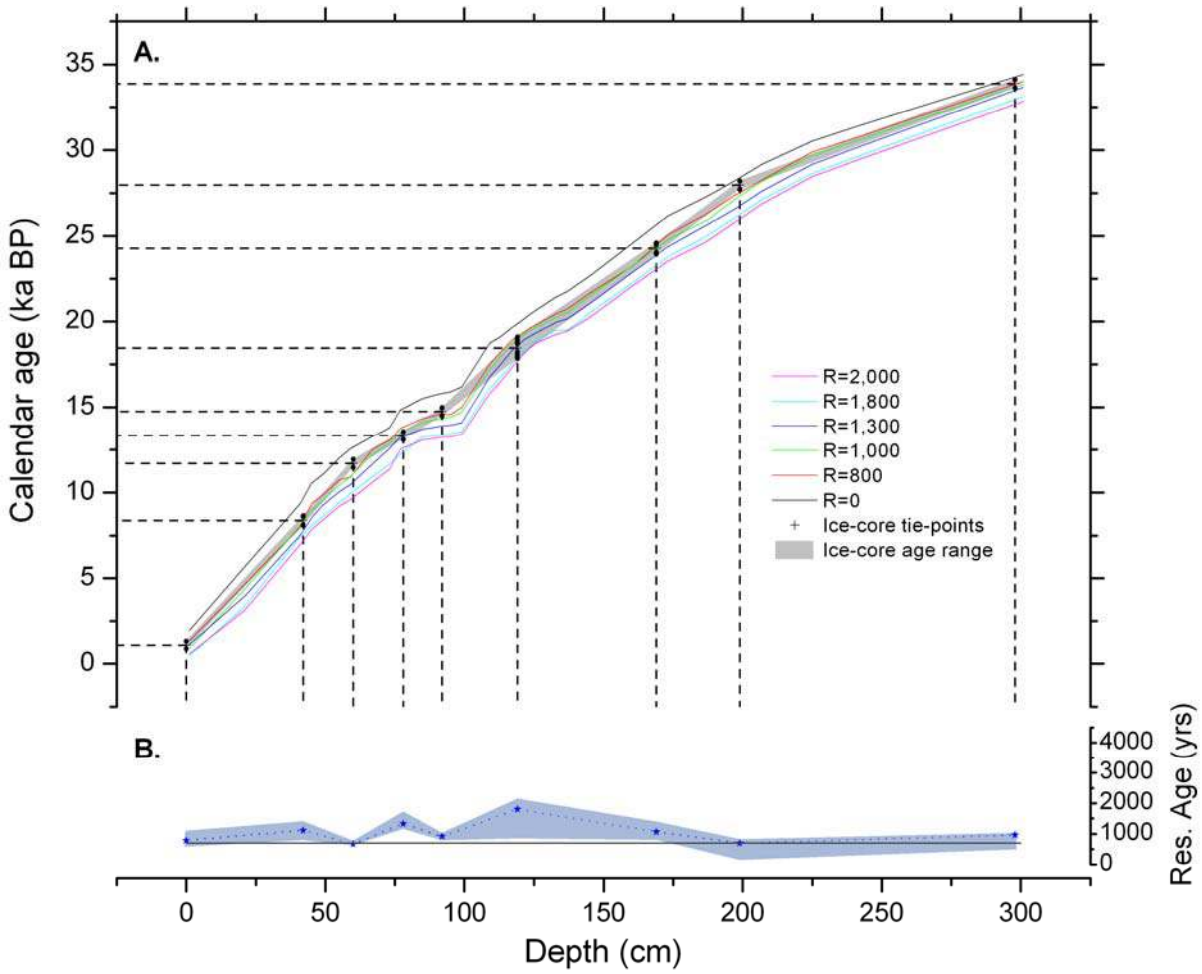


**Figure S4.** Assessment of surface reservoir ages for MD07-3076 inferred from the ice-core chronology illustrated in Figure S3. **(A)** Comparison of ice-core chronology tie-points (black crosses and dashed drop-lines) with possible calibrated radiocarbon age-scales that have been derived using the calibration datasets of (*S19, S20*) and statistical treatment of (*S23*) combined with a range of different surface reservoir age corrections on the planktonic $^{14}C$ dataset from MD07-3076 (coloured lines; uppermost represents limit of zero reservoir age correction; lower-most includes 2,000 year reservoir age correction). The age-range spanning the ice-core uncertainty limits is shown by the grey shaded area. **(B)** Median (stars and dashed blue line) and maximum/minimum (shaded area) reservoir age estimates for core MD07-3076 derived from the ice-core age ranges. Horizontal line indicates a constant modern reservoir age of 700 years for comparison.

**Figure S5.**

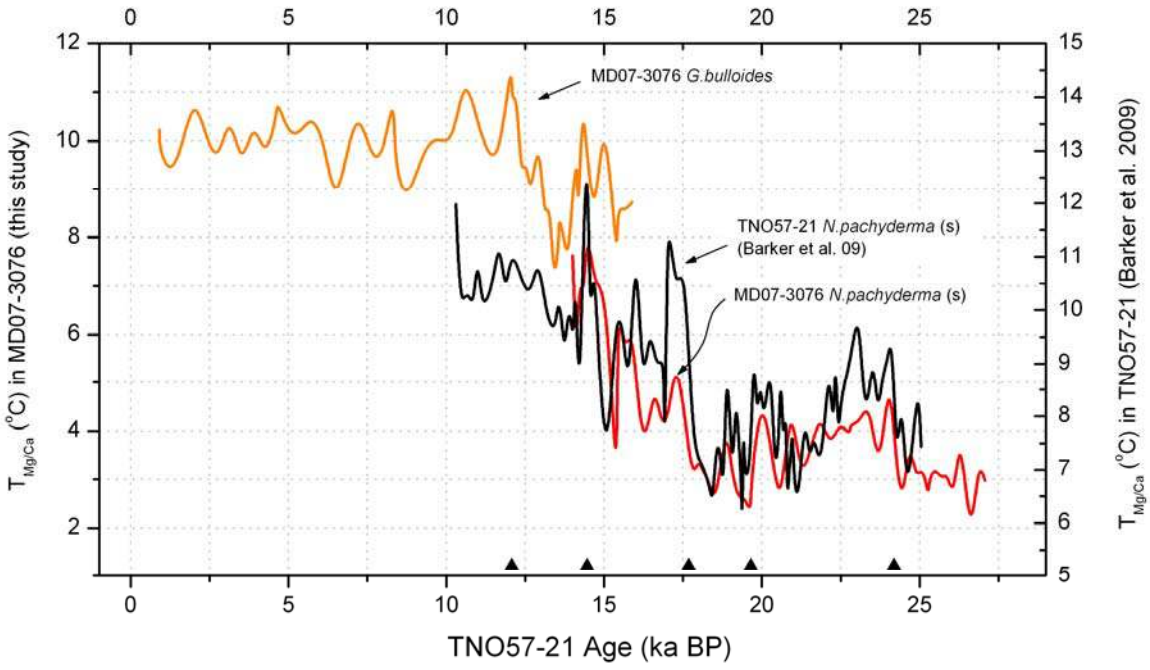


**Figure S5.** Correlation of Mg/Ca temperature reconstructions in cores MD07-3076 (this study) and TNO57-21 (*S22*). Tie points are indicated by black triangles.

**Figure S6.**

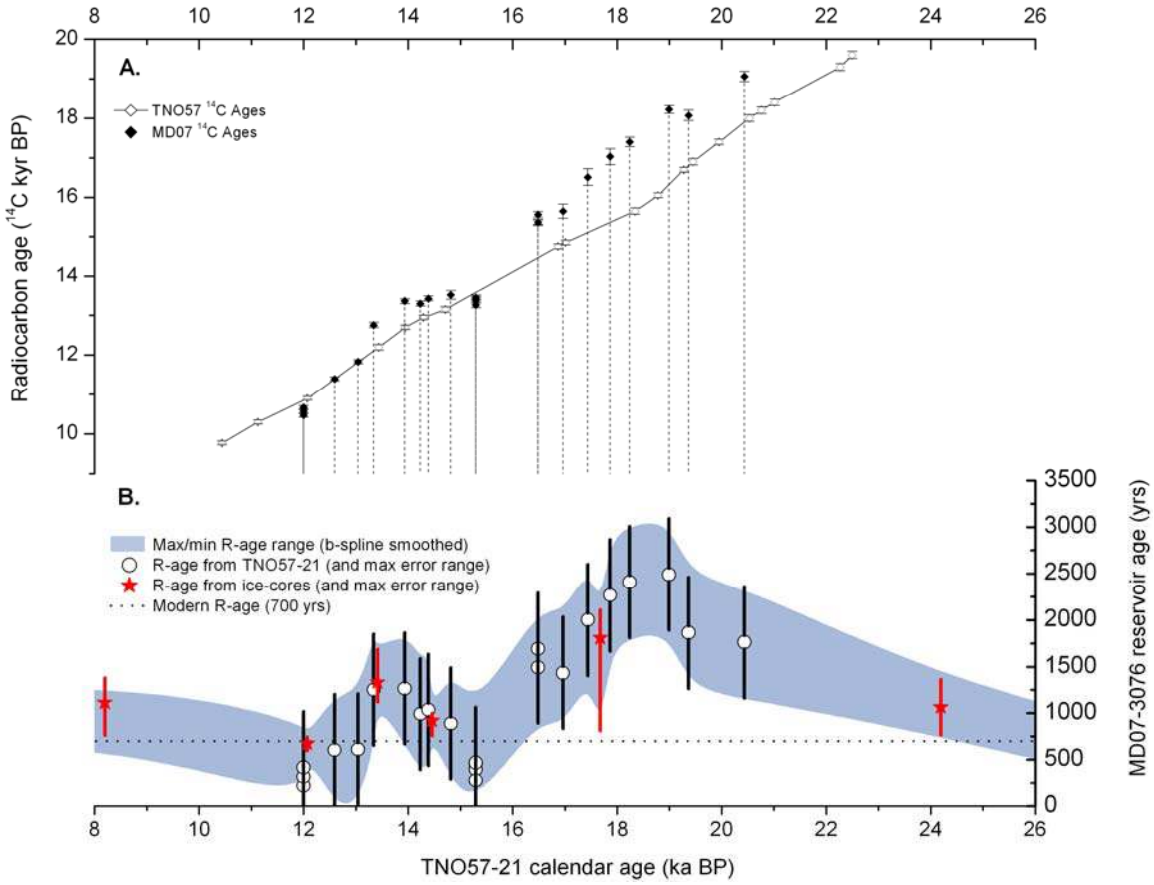


**Figure S6.** Inferred surface-water reservoir ages in MD07-3076 derived from the correlation with TNO57-21. **(A)** Radiocarbon ages (no reservoir age corrections) in MD07-3076 (filled diamonds) and from TNO57-21 (open diamonds, joined by solid line), both with 1σ-uncertainties. These data are shown on the age-scale of TNO57-21 (*S22*), adopted for the MD07-3076 data via the correlation shown in Figure S5. **(B)** Surface-water reservoir ages for MD07-3076 inferred from: 1) the radiocarbon-age offset between the two cores plus the constant reservoir age of 600 years that has been applied in TNO57-21 (open circles, with vertical error ranges of 600 years); and 2) the ice-core tie-points shown in Fig S4B (filled stars, with vertical error ranges). The radiocarbon age offsets were obtained by interpolating radiocarbon ages in TNO57-21 at the chronological position of radiocarbon ages in MD07-3076 (dashed vertical lines in A). The horizontal line in B shows a constant modern reservoir age of 700 years for comparison.

**Fig S7.**

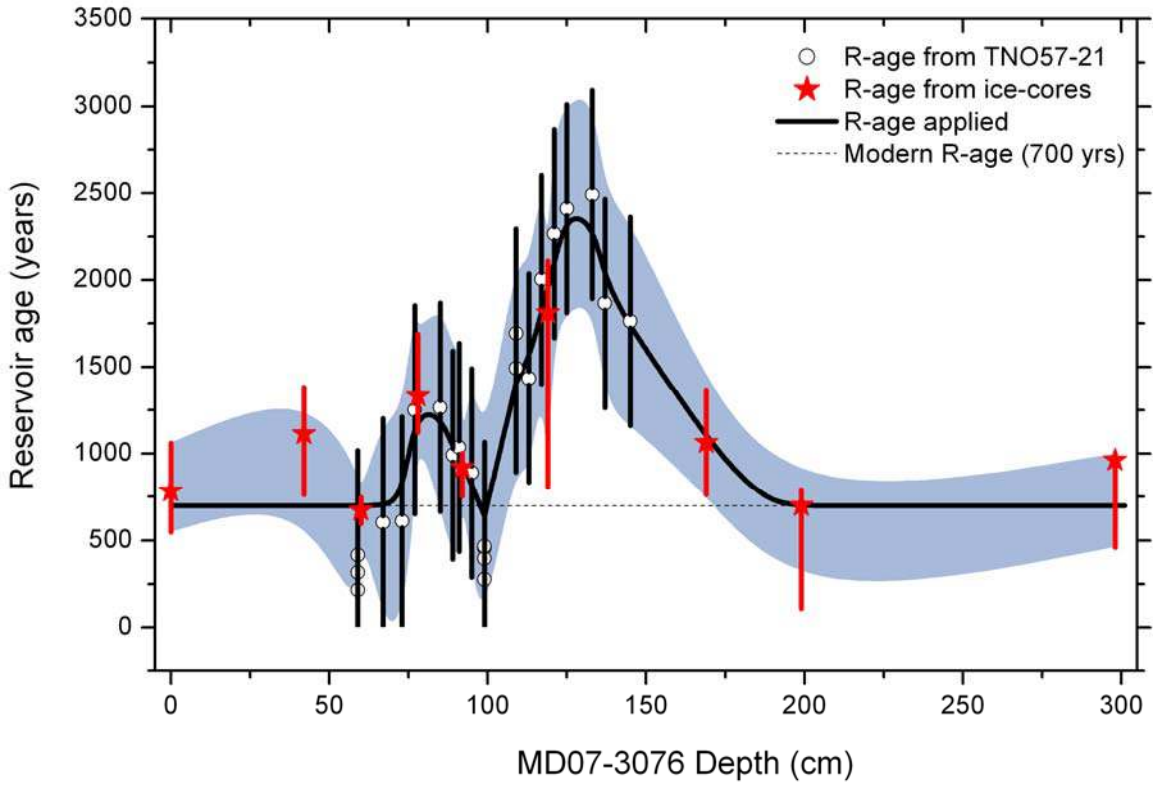


**Figure S7.** Summary of reservoir age estimates and associated uncertainty limits for core MD07-3076. Red stars and vertical bars indicate ice-core derived reservoir age estimates and associated uncertainty range (see SOM text); open black circles and vertical bars indicate reservoir age estimates derived from correlation with TNO57-21 and associated error range (± 600 years, with truncation at zero). The shaded area is defined by b-spline smoothed lines running through the upper- and lower reservoir age limits. The dashed horizontal line indicates a constant modern reservoir age of 700 years; the heavy black line indicates the best estimate reservoir age scenario applied in core MD07-3076.

**Figure S8.**

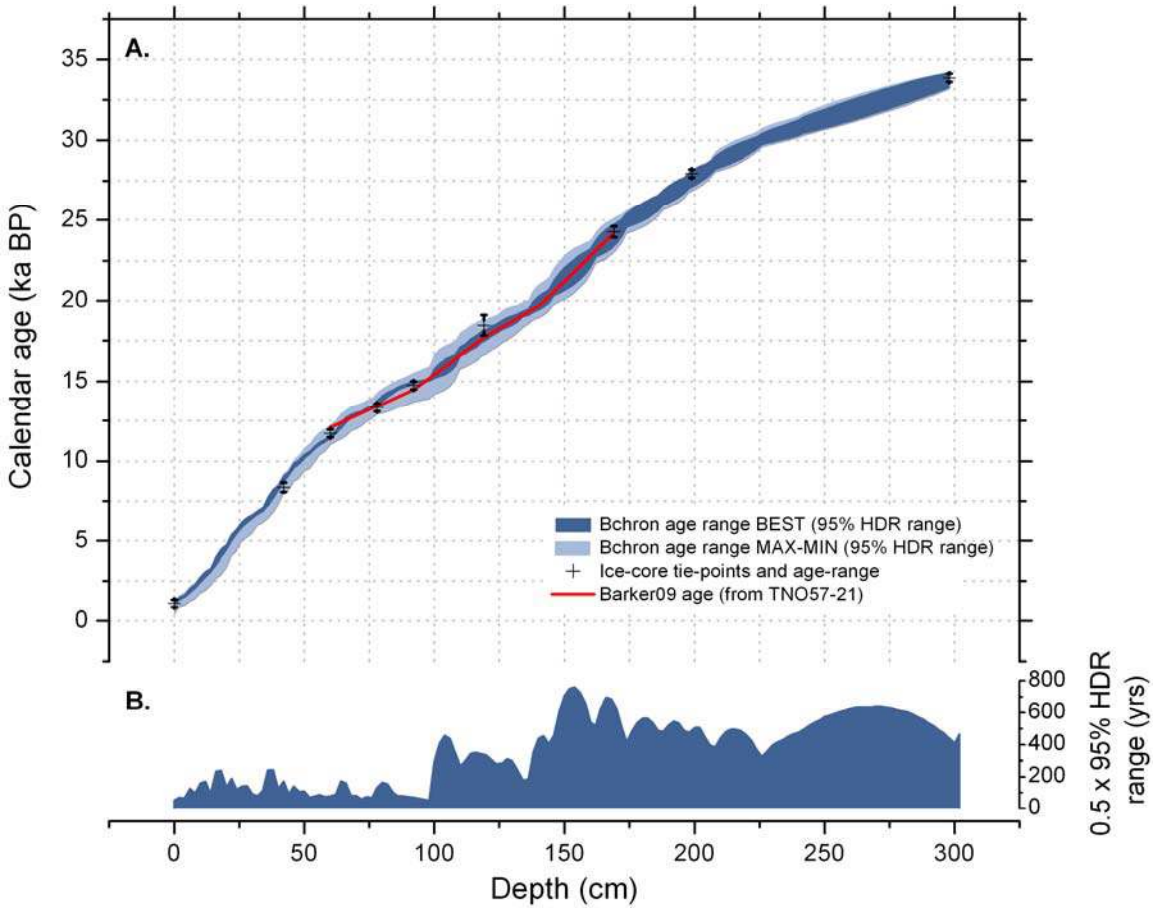


**Figure S8. A.** Comparison of different calendar chronologies and associated error ranges for core MD07-3076, based on: 1) correlation with the Antarctic EDML ice-core (black crosses with vertical error bars); 2) correlation with TNO57-21 and adoption of its calibrated radiocarbon chronology (*S22*) (solid red line); and 3) calibration of the planktonic radiocarbon dates from MD07-3076 using variable reservoir ages that are consistent with both of the above sets of chronostratigraphic constraints (see Fig S7), followed by age-depth modelling using *Bchron* (dark/light blue shaded area, indicating the 2.5-97.5% highest posterior density region, i.e. the 95% HDR range). The dark blue shaded region indicates the 95% HDR range for the best estimate reservoir age scenario and chronology. The light blue shaded area indicates the range between the 2.5% HDR of the maximum reservoir age scenario and the 97.5% HDR of the minimum reservoir age scenario (see SOM text). **B.** Half of the 2.5-97.5% HDR for the best chronology estimate (dark blue shaded region in A).

**Table S1.** Planktonic radiocarbon dates from MD07-3076.

| Depth cm | Best Bchron cal. Age (yrs BP) yrs BP | Half ± 95% HDR yrs | Planktonic Dates | | | | | |
|---|---|---|---|---|---|---|---|---|
| | | | Species | AMS Lab Code | $^{14}$C age $^{14}$C yrs BP | ± 1σ | Best estimate reservoir age yrs | Reservoir corr. $^{14}$C Age $^{14}$C yrs BP |
| 1 | 1042 | 46 | *G.bull* | 2329 | 1985 | 30 | 700 | 1,285 |
| 1 | 1042 | 46 | *G.inflata* | 2330 | 2475 | 30 | 700 | 1,775 |
| 5 | 1458 | 93 | *G.bull* | SUERC-25165 | 2362 | 35 | 700 | 1,662 |
| 9 | 1991 | 116 | *G.bull* | SUERC-25166 | 2945 | 37 | 700 | 2,245 |
| 15 | 2986 | 162 | *G.bull* | SUERC-25167 | 3725 | 37 | 700 | 3,025 |
| 21 | 4329 | 162 | *G.bull* | 2331 | 4905 | 35 | 700 | 4,205 |
| 25 | 5370 | 139 | *G.bull* | SUERC-25170 | 5687 | 37 | 700 | 4,987 |
| 31 | 6319 | 93 | *G.bull* | SUERC-25171 | 6506 | 37 | 700 | 5,806 |
| 35 | 6806 | 185 | *G.bull* | SUERC-25172 | 6732 | 36 | 700 | 6,032 |
| 41 | 8079 | 162 | *G.bull* | 2332 | 8390 | 40 | 700 | 7,690 |
| 45 | 9074 | 116 | *G.inflata* | 3838 | 9520 | 40 | 700 | 8,820 |
| 45 | 9074 | 116 | *G.inflata* | 3819 | 9510 | 50 | 700 | 8,810 |
| 45 | 9074 | 116 | *G.bull* | 3818 | 9070 | 50 | 700 | 8,370 |
| 49 | 9769 | 116 | *G.bull* | 2333 | 9560 | 40 | 700 | 8,860 |
| 53 | 10347 | 69 | *G.bull* | 12329 | 9790 | 50 | 700 | 9,090 |
| 53 | 10347 | 69 | *G.inflata* | 12330 | 10060 | 50 | 700 | 9,360 |
| 55 | 10694 | 69 | *G.bull* | 2335 | 10300 | 45 | 700 | 9,600 |
| 59 | 11134 | 69 | *G.bull* | 3823 | 10470 | 50 | 700 | 9,770 |
| 59 | 11134 | 69 | *G.inflata* | 3905 | 10570 | 60 | 700 | 9,870 |
| 59 | 11134 | 69 | *G.inflata* | 3824 | 10670 | 50 | 700 | 9,970 |
| 61 | 11389 | 93 | *G.bull* | 12335 | 10600 | 50 | 700 | 9,900 |
| 61 | 11389 | 93 | *G.inflata* | 12336 | 10730 | 50 | 700 | 10,030 |
| 63 | 11644 | 116 | *G.bull* | 12337 | 10790 | 50 | 700 | 10,090 |
| 63 | 11644 | 116 | *G.inflata* | 12338 | 10820 | 50 | 700 | 10,120 |
| 67 | 12222 | 139 | *G.bull* | 2336 | 11400 | 50 | 700 | 10,700 |
| 73 | 12894 | 69 | *G.bull* | 2337 | 11835 | 50 | 700 | 11,135 |
| 77 | 13241 | 93 | *G.bull* | 2414 | 12760 | 60 | 1251 | 11,509 |
| 85 | 14097 | 93 | *G.bull* | 2416 | 13360 | 60 | 700 | 12,660 |
| 89 | 14491 | 69 | *G.bull* | 2417 | 13300 | 60 | 700 | 12,600 |
| 91 | 14653 | 69 | *G.bull* | 2418 | 13430 | 60 | 700 | 12,730 |
| 95 | 14792 | 69 | *G.bull* | 3825 | 13520 | 110 | 700 | 12,820 |
| 99 | 15139 | 162 | *G.inflata* | 3827 | 13440 | 60 | 700 | 12,740 |
| 99 | 15139 | 162 | *G.inflata* | 3906 | 13380 | 60 | 700 | 12,680 |
| 99 | 15139 | 162 | *G.inflata* | 5007 | 13380 | 70 | 700 | 12,680 |
| 99 | 15139 | 162 | *G.inflata* | 5009 | 13450 | 60 | 700 | 12,750 |
| 99 | 15139 | 162 | *G.inflata* | 5010 | 13260 | 60 | 700 | 12,560 |
| 109 | 16574 | 324 | *G.inflata* | 3812 | 15360 | 70 | 1411 | 13,949 |
| 109 | 16574 | 324 | *G.inflata* | 5214 | 15360 | 60 | 1411 | 13,949 |
| 109 | 16574 | 324 | *N.pac(l)* | 5216 | 15560 | 80 | 1411 | 14,149 |
| 113 | 17106 | 324 | *N.pac(l)* | 5206 | 15650 | 180 | 1550 | 14,100 |
| 117 | 17569 | 347 | *N.pac(l)* | 5207 | 16510 | 210 | 1812 | 14,698 |
| 119 | 17801 | 347 | *G.bull* | SUERC-25631 | 16698 | 50 | 1684 | 15,014 |
| 121 | 18009 | 324 | *N.pac(l)* | 5209 | 17030 | 200 | 2097 | 14,933 |
| 125 | 18380 | 278 | *N.pac(l)* | 3816 | 17400 | 120 | 2387 | 15,013 |
| 133 | 19028 | 231 | *N.pac(l)* | 2424 | 18220 | 100 | 2340 | 15,880 |
| 137 | 19398 | 255 | *N.pac(l)* | 2425 | 18070 | 130 | 1997 | 16,073 |
| 145 | 20509 | 440 | *N.pac(l)* | 2426 | 19060 | 130 | 1727 | 17,333 |
| 161 | 22870 | 532 | *N.pac(l)* | 2427 | 20580 | 130 | 1307 | 19,273 |
| 173 | 24722 | 463 | *G.inflata* | 3830 | 21730 | 100 | 700 | 21,030 |
| 187 | 26,227 | 486 | G.inflata | 2429 | 22440 | 160 | 700 | 21,740 |
| 197 | 27,384 | 486 | G.inflata | 3831 | 23390 | 110 | 700 | 22,690 |
| 207 | 28,472 | 394 | G.inflata | 2430 | 24520 | 200 | 700 | 23,820 |
| 219 | 29,468 | 463 | N.pac(l) | SUERC-25640 | 25407 | 85 | 700 | 24,707 |
| 225 | 29,931 | 347 | G.inflata | 3833 | 25970 | 130 | 700 | 25,270 |
| 241 | 30,810 | 486 | N.pac(l) | 2432 | 26550 | 250 | 700 | 25,850 |
| 265 | 32,106 | 625 | N.pac(l) | SUERC-25642 | 28540 | 89 | 700 | 27,840 |
| 275 | 32,639 | 625 | N.pac(l) | SUERC-25644 | 28827 | 91 | 700 | 28,127 |
| 301 | 34,167 | 440 | N.pac(l) | 2433 | 30140 | 370 | 700 | 29,440 |
| 301 | 34,167 | 440 | G.inflata | 3836 | 30250 | 180 | 700 | 29,550 |

* no online $\delta^{13}$C measurement made (AMS dates corrected for $\delta^{13}$C = 0 ± 2 ‰)

.

**Table S2.** Benthic radiocarbon dates, B-P offsets and apparent ventilation age estimates from MD07-3076.

| | | | Benthic Dates | | | | Paired Planktonic Dates | | | Ventilation Age estimates | | | Chronology and ventilation age ranges | | | |
|---|---|---|---|---|---|---|---|---|---|---|---|---|---|---|---|---|
| Depth cm | Best Bchron cal. Age (yrs BP) yrs BP | Half ± 95% HDR yrs | Species | AMS Lab Code | Benthic $^{14}$C age $^{14}$C yrs BP | ± 1σ | Mean Planktonic $^{14}$C age $^{14}$C yrs BP | ± 1σ | Best estimate reservoir age yrs | B-P yrs | ± 1σ | Best App. ventilation age (B-Atm) yrs | MIN R Bchron cal. Age (yrs BP) yrs BP | B-Atm (MIN R) yrs | MAX R Bchron cal. Age (yrs BP) yrs BP | B-Atm (MAX R) yrs |
| 1 | 1,042 | 46 | Benthics | 2530 | 3210 | 40 | 2,230 | 30 | 700 | 980 | 70 | 1,680 | 1,319 | 1,461 | 833 | 2,119 |
| 5 | 1,458 | 93 | Benthics | SUERC-25177 | 3366 | 35 | 2,362 | 35 | 700 | 1,004 | 70 | 1,704 | 1,759 | 1,506 | 1,227 | 2,174 |
| 15 | 2,986 | 162 | Benthics | SUERC-25182 | 4659 | 37 | 3,725 | 37 | 700 | 934 | 74 | 1,634 | 3,356 | 1,480 | 2,708 | 2,181 |
| 21 | 4,329 | 162 | Benthics | 2437 | 5800 | 45 | 4,905 | 35 | 700 | 895 | 80 | 1,595 | 4,815 | 1,453 | 4,028 | 2,185 |
| 31 | 6,319 | 93 | Benthics | SUERC-25183 | 7289 | 36 | 6,506 | 37 | 700 | 783 | 73 | 1,482 | 6,644 | 1,347 | 6,019 | 2,107 |
| 35 | 6,806 | 185 | Benthics | SUERC-25184 | 7409 | 36 | 6,732 | 36 | 700 | 677 | 72 | 1,378 | 7,176 | 1,227 | 6,667 | 2,006 |
| 41 | 8,079 | 162 | Benthics | 2532 | 9120 | 45 | 8,390 | 40 | 700 | 730 | 85 | 1,430 | 8,588 | 1,209 | 7,917 | 2,056 |
| 45 | 9,074 | 116 | Benthics | 3820 | 9780 | 60 | 9,367 | 47 | 700 | 413 | 107 | 1,113 | 9,537 | 804 | 8,657 | 1,727 |
| 53 | 10,347 | 69 | Benthics | 12320 | 10875 | 60 | 9,925 | 71 | 700 | 950 | 131 | 1,650 | 11,019 | 1,120 | 10,023 | 2,149 |
| 55 | 10,694 | 69 | Benthics | 2434 | 11440 | 60 | 10,300 | 45 | 700 | 1,140 | 105 | 1,840 | 11,389 | 1,284 | 10,394 | 2,257 |
| 59 | 11,134 | 69 | Benthics | 3821 | 11810 | 60 | 10,570 | 53 | 700 | 1,240 | 113 | 1,940 | 11,921 | 1,410 | 10,926 | 2,215 |
| 61 | 11,389 | 93 | Benthics | 12321 | 11437 | 70 | 10,665 | 71 | 700 | 772 | 141 | 1,472 | 12,222 | 1,029 | 11,157 | 1,764 |
| 63 | 11,644 | 116 | Benthics | 12323 | 11780 | 50 | 10,805 | 71 | 700 | 975 | 121 | 1,675 | 12,523 | 1,177 | 11,366 | 2,043 |
| 67 | 12,222 | 139 | Benthics | 2439 | 12230 | 60 | 11,400 | 50 | 700 | 830 | 110 | 1,530 | 13,102 | 817 | 11,898 | 2,073 |
| 73 | 12,894 | 69 | Benthics | 2533 | 12690 | 60 | 11,835 | 50 | 700 | 855 | 110 | 1,555 | 13,565 | 884 | 12,523 | 2,304 |
| 77 | 13,241 | 93 | Benthics | 2535 | 13200 | 60 | 12,760 | 60 | 1,251 | 440 | 120 | 1,691 | 13,912 | 1,068 | 12,894 | 2,314 |
| 85 | 14,097 | 93 | Benthics | 2536 | 13680 | 70 | 13,360 | 60 | 700 | 320 | 130 | 1,020 | 14,792 | 855 | 13,380 | 2,235 |
| 85 | 14,097 | 93 | Benthics | 2537 | 13810 | 70 | 13,360 | 60 | 700 | 450 | 130 | 1,150 | 14,792 | 985 | 13,380 | 2,365 |
| 89 | 14,491 | 69 | Benthics | 2505 | 13930 | 80 | 13,300 | 60 | 700 | 630 | 140 | 1,330 | 15,116 | 924 | 13,588 | 2,404 |
| 91 | 14,653 | 69 | Benthics | 2506 | 14080 | 90 | 13,430 | 60 | 700 | 650 | 150 | 1,350 | 15,255 | 1,001 | 13,727 | 2,290 |
| 95 | 14,792 | 69 | Benthics | 2507 | 14000 | 100 | 13,520 | 110 | 700 | 480 | 210 | 1,180 | 15,532 | 608 | 13,889 | 2,015 |
| 99 | 15,139 | 162 | Benthics | 2509 | 15050 | 80 | 13,382 | 62 | 700 | 1,668 | 142 | 2,368 | 15,949 | 1,697 | 14,167 | 3,051 |
| 101 | 15,509 | 347 | Benthics | 12324 | 14910 | 60 | | | 700 | | | | 16,273 | | 14,514 | |
| 103 | 15,764 | 440 | Benthics | 12325 | 15250 | 60 | | | 700 | | | | 16,528 | | 14,815 | |
| 105 | 15,995 | 440 | Benthics | 2510 | 16020 | 80 | | | 700 | | | | 16,782 | | 15,116 | |
| 109 | 16,574 | 324 | Benthics | 3812 | 16560 | 70 | 15,427 | 70 | 1,421 | 1,133 | 140 | 2,554 | 17,431 | 1,824 | 15,764 | 3,285 |
| 113 | 17,106 | 324 | Benthics | 3804 | 17010 | 70 | 15,650 | 180 | 1,550 | 1,360 | 250 | 2,910 | 17,963 | 2,060 | 16,273 | 3,760 |
| 117 | 17,569 | 347 | Benthics | 2511 | 17750 | 100 | 16,510 | 210 | 1,812 | 1,240 | 310 | 3,052 | 18,356 | 2,131 | 16,713 | 3,974 |
| 119 | 17,801 | 347 | Benthics | SUERC-25185 | 17874 | 42 | 16,698 | 50 | 1,684 | 1,176 | 92 | 2,861 | 18,565 | 2,135 | 16,944 | 3,588 |
| 121 | 18,009 | 324 | Benthics | 3809 | 17640 | 80 | 17,030 | 200 | 2,097 | 610 | 280 | 2,707 | 18,727 | 1,815 | 17,153 | 3,599 |
| 125 | 18,380 | 278 | Benthics | 3805 | 18490 | 70 | 17,400 | 120 | 2,387 | 1,090 | 190 | 3,477 | 18,958 | 2,686 | 17,593 | 4,267 |
| 133 | 19,028 | 231 | Benthics | 2512 | 19530 | 120 | 18,220 | 100 | 2,340 | 1,310 | 220 | 3,650 | 19,630 | 2,830 | 18,565 | 4,470 |
| 137 | 19,398 | 255 | Benthics | 2513 | 19870 | 130 | 18,070 | 130 | 1,997 | 1,800 | 260 | 3,797 | 19,977 | 2,937 | 18,889 | 4,657 |
| 145 | 20,509 | 440 | Benthics | 2514 | 20800 | 130 | 19,060 | 130 | 1,728 | 1,740 | 260 | 3,468 | 21,134 | 2,635 | 19,954 | 4,300 |
| 161 | 22,870 | 532 | Benthics | 2517 | 22270 | 180 | 20,580 | 130 | 1,306 | 1,690 | 310 | 2,996 | 23,426 | 2,269 | 22,384 | 3,723 |
| 173 | 24,722 | 463 | Benthics | 2518 | 23180 | 180 | 21,730 | 100 | 700 | 1,450 | 280 | 2,150 | 24,954 | 1,831 | 24,282 | 3,063 |
| 187 | 26,227 | 486 | Benthics | 2519 | 24470 | 210 | 22,440 | 160 | 700 | 2,030 | 370 | 2,730 | 26,065 | 2,094 | 25,833 | 3,439 |
| 197 | 27,384 | 486 | Benthics | 3924 | 24690 | 150 | 23,390 | 110 | 700 | 1,300 | 260 | 2,000 | 26,551 | 1,379 | 27,060 | 2,490 |
| 207 | 28,472 | 394 | Benthics | 2520 | 26080 | 240 | 24,520 | 200 | 700 | 1,560 | 440 | 2,260 | 28,426 | 1,408 | 28,218 | 2,873 |
| 225 | 29,931 | 347 | Benthics | 3926 | 26960 | 130 | 25,970 | 130 | 700 | 990 | 260 | 1,690 | 30,162 | 994 | 29,815 | 2,091 |
| 241 | 30,810 | 486 | Benthics | 2523 | 28670 | 310 | 26,550 | 250 | 700 | 2,120 | 560 | 2,820 | 31,065 | 1,844 | 30,648 | 3,531 |

**Table S3.** Benthic radiocarbon dates and apparent ventilation age estimates from core MD99-2334K

| Corrected depth cm | Calendar Age ** yr BP | Species | Lab number | $^{14}$C age yr BP | ± | Apprent ventilation age (B-Atm) years |
|---|---|---|---|---|---|---|
| 2 | 710 | mixed benthics | SSAMS ANU #3935 | 1,300 | 40 | 1,148 |
| 109 | 11,306 | mixed benthics | SSAMS ANU #2526 | 11,470 | 70 | 1,458 |
| 115 | 12,140 | mixed benthics | * Gif 102647 | 11,800 | 150 | 1,448 |
| 149 | 14,196 | mixed benthics | * Gif 102648 | 13,230 | 150 | 887 |
| 150 | 14,293 | mixed benthics | * Gif 102649 | 13,290 | 130 | 905 |
| 173 | 15,341 | mixed benthics | * Gif 102222 | 15,220 | 140 | 2,209 |
| 186 | 15,956 | mixed benthics | * Gif 102650 | 15,940 | 150 | 2,512 |
| 241 | 18,511 | mixed benthics | SSAMS ANU #2614 | 17,100 | 120 | 2,080 |
| 313 | 22,219 | mixed benthics | * Gif 102651 | 20,370 | 180 | 1,376 |

** Calendar age-scale is from (*S25*). * Data previously published in (*S7*).

**References**


S1. B. Sloyan, S. R. Rintoul, *J Phys Oceanogr* **31**, 143 (2001).

S2. J. R. Reid, in *The South Atlantic: Present and Past Circulation,* G. Wefer, A. Berger, G. Siedler, D. J. Webb, Eds. (Springer-Verlag, Berlin Heidelberg, 1996), pp. 13-44.

S3. K. Matsumoto, *Journal of Geophysical Research* **112**, 1 (2007).

S4. D. Iudicone, S. Speich, G. Madec, B. Blanke, *J Phys Oceanogr* **38**, 1401 (2008).

S5. G. Mortyn, C. D. Charles, *Paleoceanography* **18**, 15.1 (2003).

S6. S. Barker, M. Greaves, H. Elderfield, *Geochem. Geophys. Geosys.* **4**, 84078 (2003).

S7. L. C. Skinner, N. J. Shackleton, *Paleoceanography* **19**, 1 (2004).

S8. S. de Villiers, M. Greaves, H. Elderfield, *Geochem. Geophys. Geosys.* **3**, 1 (2002).

S9. M. Greaves *et al.*, *Geochem. Geophys. Geosys.* **9**, doi:10.1029/2008GC001974 (2008).

S10. S. J. Brown, H. Elderfield, *Paleoceanography* **11**, 543 (1996).

S11. T. A. Mashiotta, D. W. Lea, H. J. Spero, *Earth Planet. Sci. Lett.* **170**, 417 (1999).

S12. P. J. von Langen, D. K. Pak, H. J. Spero, D. W. Lea, *Geochem. Geophys. Geosys.* **6**, 1 (2005).

S13. W. L. Prell, "The stability of low-latitude sea-surface temperatures: An evaluation of the CLIMAP reconstruction with emphasis on the positive SST anomalies" (United States Department of Energy, 1985).

S14. A. Govin *et al.*, *Paleoceanography* **24**, PA1202 (2009).

S15. B. Lemieux-Dudon *et al.*, *Quat. Sci. Rev.* **29**, 8 (2010).

S16. E. Monnin *et al.*, *Science* **291**, 112 (2001).

S17. H. J. Smith, H. Fischer, M. Wahlen, D. Mastroianni, B. Deck, *Nature* **400**, 248 (15 July 1999, 1999).

S18. T. M. Marchitto, S. J. Lehman, J. D. Otiz, J. Fluckiger, A. van Geen, *Science* **316**, 1456 (2007).

S19. P. J. Reimer *et al.*, *Radiocarbon* **46**, 1029 (2004).

S20. K. Hughen, J. Southon, S. Lehman, C. Bertrand, J. Turnbull, *Quat. Sci. Rev.* **25**, 3216 (2006).

S21. R. M. Key *et al.*, *Global Biogeochem. Cycles* **18**, 1 (2004).

S22. S. Barker *et al.*, *Nature* **457**, 1097 (2009).

S23. A. C. Parnell, J. Haslett, J. R. M. Allen, C. E. Buck, B. Huntley, *Quat. Sci. Rev.* **27**, 1872 (2008).

S24. W. Broecker, S. Barker, *Earth Planet. Sci. Lett.* **256**, 90 (2007).

S25. L. C. Skinner, *Clim. Past* **4**, 295 (2008).

S26. D. Olbers, V. V. Gouretski, G. Siess, J. Schroter, “Hydrographic Atlas of the Southern Ocean” (Alfred Wegener Institute for Polar and Marine Research, Bremerhaven, Germany/Arctic and Antarctic Research Institute of St. Petersburg, Russia, 1992).

S27. A. H. Orsi, T. Whitworth III, W. D. Nowlin Jr., *Deep-Sea Research I* **42**, 641 (1995).

S28. A. H. Orsi, G. C. Johnson, J. L. Bullister, *Prog. Oceanogr.* **43**, 55 (1999).